Geophysical Journal International

Geophys. J. Int. (2026) **245,** 1–24
Advance Access publication 2026 March 13
Research Paper

https://doi.org/10.1093/gji/ggag088

Estimating subsurface velocity and resonance frequency changes using two decades of KiK-net data in the Iwate Prefecture, Japan

Alessandra Schibuola [1], Ssu-Ting Lai [2], Luis Fabián Bonilla [1], Eléonore Stutzmann [3] and Martin Schimmel [4]

[1] *Université Gustave Eiffel , Département GERS (Géotechnique, Environnement, Risques naturels et Sciences de la terre), Cité Descartes, F-77447Marne-la-Vallée Cedex 2, France. E-mail: alessandra.schibuola97@gmail.com*
[2] *GFZ Helmholtz Centre for Geosciences, , D-14473 Potsdam, Germany,*
[3] *Université Paris Cité, Institut de physique du globe de Paris, CNRS,* F-75005 *Paris, France*
[4] *Geosciences Barcelona—CSIC, Lluis Sole i Sabaris s/n,* E-08028 *Barcelona, Spain*

Accepted 2026 February 26. Received 2026 February 20; in original form 2025 September 10

SUMMARY

Earthquake ground motion is strongly influenced by near-surface geology, which governs its amplification, duration and spatial variability. Under intense shaking and depending on the material strength, sediments often exhibit nonlinear behaviour, producing large deformations that reduce shear-wave velocity, shift resonance frequencies and increase damping. We analyse over two decades of borehole–surface recordings from 28 stations in Iwate Prefecture, Japan, collected by the Kiban Kyoshin network (KiK-net), to quantify these effects. Frequency-domain analysis (stacked Stockwell power spectral density) and time-domain interferometric methods (multitaper deconvolution and phase cross-correlation) provide consistent results, revealing systematic decreases in both resonance frequency and seismic velocity with increasing peak ground acceleration (PGA). Frequency shifts inferred from the surface data mainly reflect the shallowest layers, whereas velocity changes estimated with borehole-referenced methods capture a path-averaged perturbation between the surface and borehole sensors and therefore depend on borehole depth. The data set is divided into seven PGA bins based on surface recordings, with the 1–5 cm s^{-2} bin serving as a baseline for comparison, representing linear site conditions. Across all stations, relative velocity reductions average $\sim$ 12 per cent in the 200–400 cm s^{-2} PGA range, corresponding to a shear modulus reduction (μ/μ_0) of about 23 per cent. Nonlinear effects are most pronounced at sites with thicker sedimentary deposits, which are mainly found in the central valley and northern foothills of Iwate Prefecture. In contrast, V_{S30} shows no clear correlation with the observed nonlinearity, as its averaging effect masks thin low-velocity layers near the surface that are prone to nonlinear response during strong shaking. These results underline that nonlinear site response is highly site-specific, and that large observational data sets are crucial for robust characterization across a seismic network.

Key words: Elasticity and anelasticity; Earthquake ground motions; Japan; Empirical Green's function; Seismic Interferometry; Site effects.

1 INTRODUCTION

The geological conditions of the shallow subsurface exert a strong influence on seismic ground shaking. Young, unconsolidated soils tend to amplify ground motion (K. Aki 1993), an effect that is particularly pronounced in sedimentary basins (J. Bustos *et al.* 2023; F. Ortiz *et al.* 2024). Sharp impedance contrasts between sediments and underlying bedrock can trap seismic waves, leading to spatial variability in both the amplitude and duration of shaking (L. Ermert *et al.* 2023). These site effects contribute to heterogeneous patterns of earthquake-induced damage, as observed in several major events, including the 1985 Mexico City earthquake (M. Celebi *et al.* 1987), the 1999 Chi-Chi earthquake in Taiwan (S.J. Lee *et al.* 2007) and the 2010 Maule earthquake in Chile (R.L. Boroschek *et al.* 2012).

Seismic amplification is commonly assumed to follow linear behaviour, wherein the shear modulus and damping remain constant regardless of strain amplitude. Under this idealized assumption, amplification is primarily governed by the impedance contrast between bedrock and overlying soft soils (S.L. Kramer 1996). However, this linear assumption breaks down under strong ground motion. Large strain levels in shallow, low-velocity layers can induce nonlinear material behaviour, typically manifested as a reduction in shear modulus and an increase in damping (K. Ishihara 1996; T. Kokusho 2004).

These nonlinear effects have been extensively characterized in laboratory settings. Since the seminal work of H.B. Seed (1970), studies have consistently shown that increasing strain results in a decrease in shear modulus and a concurrent increase in damping

(B.O. Hardin & V.P. Drnevich 1972; K. Ishihara *et al.* 1985). The shear modulus (μ) is defined as $\mu = \rho V_S^2$, where ρ is the material density and V_S the shear-wave velocity. Thus, a reduction in shear modulus corresponds to a decrease in V_S (I.A. Beresnev & K.L. Wen 1996). Laboratory tests have also revealed that increasing strain leads to a downward shift in resonance frequency (J.A. TenCate *et al.* 2004; D. Pasqualini *et al.* 2007), which directly reflects reduced stiffness and slower wave propagation.

Despite robust laboratory evidence, *in situ* confirmation of nonlinear site response remains challenging. These difficulties arise from limited strong-motion data, incomplete knowledge of near-surface dynamic properties and inadequate signal quality (I.A. Beresnev & K.L. Wen 1996). Moreover, isolating local site effects from source and path influences is nontrivial (J. Aguirre & K. Irikura 1997; T. Satoh *et al.* 1997).

To address this, spectral ratio techniques are commonly employed. Empirical transfer functions require a reference site with minimal site effects (e.g. J.H. Steidl *et al.* 1996; T. Satoh *et al.* 1997). The horizontal-to-vertical spectral ratio (HVSR) method avoids this requirement but has its own limitations, such as the vertical component being affected by site conditions, and the method's limited sensitivity beyond the fundamental frequency (L.F. Bonilla *et al.* 2002). To overcome these constraints, S.T. Lai *et al.* (2025b) proposed a time-frequency resonance analysis (TFRA) method that enables broad-band tracking of site resonance frequencies, including higher modes beyond the fundamental.

A growing body of research has demonstrated evidence of nonlinearity in earthquake recordings. For example, J. Régnier *et al.* (2013) compared empirical transfer functions from the 2011 Tohoku-Oki earthquake with those from low-amplitude motions, showing resonance frequency shifts to lower values and diminished high-frequency amplification. At the same time, amplification at lower frequencies was enhanced (e.g. J. Régnier *et al.* 2016). These effects mainly reflect the nonlinear response of shallow layers, which govern the high-frequency behaviour of ground motion (T. Kokusho 2004; S.T. Lai *et al.* 2025b). Their softening reduces amplification at high frequencies and shifts resonance towards lower frequencies (L. Viens *et al.* 2022). Furthermore, M. Hallo *et al.* (2025) reported coseismic drops in frequency during the 2024 Noto earthquake using HVSR. Y.P. Dhakal *et al.* (2019) examined the 2018 Hokkaido Eastern Iburi earthquake and identified nonlinear changes in site response using both HVSR and surface-to-borehole spectral ratios (SBSR), showing reduced amplification at intermediate frequencies near the epicentre. More recently, Y.P. Dhakal *et al.* (2025) applied the same approach to the 2024 Noto earthquake and showed that the degree of nonlinearity (DNL), derived from HVSR and SBSR, increases positively with ground acceleration.

Comparing low- and high-amplitude ground motions offers a practical means of distinguishing between linear and nonlinear site responses. However, defining the threshold at which nonlinearity becomes notable remains contentious. Thresholds are often selected ad hoc based on peak ground acceleration (PGA) at the surface. For example, I.A. Beresnev & K.L. Wen (1996) suggested a range of 100–200 cm s^{-2}, for the onset of nonlinear effects, whereas other studies have suggested significantly lower thresholds, in the range of 20–50 cm s^{-2} (C. Wu *et al.* 2010; J. Régnier *et al.* 2013). The precise shaking level at which soils transition to nonlinear behaviour remains an open question.

A drop in resonance frequency following strong shaking implies a reduction in shear-wave velocity, which can be estimated as $\Delta v/v = \Delta f/f$ (L.F. Bonilla & Y. Ben-Zion 2020), under the assumption of a uniform velocity change within the medium. This proxy indicates loss of stiffness and structural compaction in near-surface materials (C. Wu *et al.* 2009; L.F. Bonilla & Y. Ben-Zion 2020; L. Viens *et al.* 2022; Z. Liu *et al.* 2022). While the shift in predominant frequency provides insight into nonlinear response, it captures only the dominant mode. S.T. Lai *et al.* (2025b) extended this approach by tracking frequency shifts across multiple modes in complex, multimodal sites. However, fully characterizing the nonlinear response across the frequency spectrum remains difficult. In this context, $\Delta v/v$ estimates from seismic interferometry offer a powerful tool to monitor time-varying material properties by capturing changes in the full waveform (R. Esfahani *et al.* 2024).

Numerous studies have observed velocity changes during strong earthquakes followed by gradual recovery, often approximated by a logarithmic trend. For instance, N. Nakata & R. Snieder (2011) reported a 22 per cent shear velocity reduction at station FKSH18 during the 2011 Tohoku-Oki earthquake, with recovery to a 10 per cent reduction the following day and 5 per cent two months later. K. Sawazaki & R. Snieder (2013) observed similar patterns at over half of their stations, noting spatial variability in the recovery process. While sites in the northern region showed full recovery within a year, the southern region—affected by stronger aftershocks—recovered more slowly. Additional examples include a 30 per cent velocity reduction (with year-long recovery) after the 2000 Western Tottori earthquake (K. Sawazaki *et al.* 2009) and an 8 per cent drop with partial recovery within two weeks following the 2019 Ridgecrest earthquake (Y. Lu & Y. Ben-Zion 2022).

These observations raise key questions: To what extent do velocity changes scale with ground shaking intensity? And how much are they modulated by site-specific conditions? This study aims to address these questions by quantifying shear-wave velocity variations as a function of both shaking level and local site characteristics.

We analyse data from the Kiban Kyoshin Network (KiK-net; S. Aoi *et al.* 2020), a dense strong-motion network in Japan. Each KiK-net station includes a pair of seismographs in a borehole configuration, allowing isolation of the site response. Our analysis focuses on 28 stations in Iwate Prefecture, which recorded a total of 42 981 earthquakes from 2000 to 2022, averaging roughly 1500 usable waveforms per station. Frequency variations are estimated through an extended version of the TFRA method (S.T. Lai *et al.* 2025b). In this work, we refer to this extended approach as the stacked Stockwell power spectral density (sSPSD), which provides a broad-band spectral characterization. Velocity changes are estimated using deconvolution-based seismic interferometry (N. Nakata & R. Snieder

2012; L.F. Bonilla *et al.* 2019; H. Zhang *et al.* 2023) and phase cross-correlation (M. Schimmel 1999), both of which exploit the borehole–surface configuration. This setup enables detailed analysis of shallow material response under varying loading conditions (L. Qin *et al.* 2020).

2 DATA AND METHODS

We use data from the Kiban Kyoshin network (KiK-net; S. Aoi *et al.* 2020), a dense strong-motion seismograph network comprising approximately 700 stations distributed uniformly across Japan since the early 2000s (National Research Institute For Earth Science And Disaster Resilience 2019). Each station features a unique dual-sensor configuration with 3-component accelerometers installed both at the surface and in boreholes, whose depths range from about 80 m to much greater values, depending on site conditions (S. Aoi *et al.* 2020). The deepest KiK-net borehole, located in Saitama Prefecture, reaches a depth of 3510 m (S. Aoi *et al.* 2020). This paired arrangement enables direct measurement of downhole and surface ground motion, facilitating isolation of near-surface site effects. Additionally, each site includes comprehensive *P*- and *S*-wave velocity profiles, providing essential subsurface characterization for site response analysis.

2.1 KiK-net sites in Iwate Prefecture

In this study, we analyse data from 28 KiK-net stations located in Iwate Prefecture, northeastern Japan (Fig. 1). These stations span a wide range of near-surface conditions, with time-averaged shear-wave velocity over the first 30 m (V_{S30}) values ranging from 300 to 1200 m s^{-1} and borehole depths between 100 and 300 m. An overview of site characteristics is provided in Table 1, while Fig. 2 presents the corresponding shear-wave velocity (V_S) profiles.

The stations installed in Iwate Prefecture span different depths as shown in Fig. 2. The velocity profiles show two families, based on their gradients. Using the theoretical vertical shear-wave traveltime down to 100 m depth, tt_{100}, we classify the sites into two groups: group A ($tt_{100} \leq 0.15$ s) and group B ($tt_{100} > 0.15$ s), depicted in Fig. 2 in grey and black, respectively. For instance, station IWTH14 has a high V_{S30} value, yet its profile reveals thin, low-velocity surface layers overlying much faster materials. This configuration results in strong near-surface velocity contrast and relatively short tt_{100}. In contrast, station IWTH12 presents a more gradual increase in velocity with depth, yielding a longer tt_{100}. Sites IWTH12 and IWTH14 are marked in Fig. 2 in blue and red, respectively. The group classification based on tt_{100} along with the corresponding values of theoretical vertical shear-wave traveltime down to the borehole (tt_{BH}) are reported in Table 1. This classification will be used later in the paper to see the effect of the velocity structure on the site's nonlinear response.

We compiled data from all Iwate Prefecture stations spanning the network's operational period since 2000 to 2022. The data set includes magnitude estimates from the Japan Meteorological Agency magnitudes (M_{JMA}) of 2.0–9.0 and recording durations of 60–300 s. Most stations have operated continuously since 2000 August 14, with three exceptions: IWTH25 (suspended in late 2009), IWTH28 (operational since 2011 March 3), and IWTH19 (suspended from 2009 to mid-2011). To ensure consistency across the data set, we resample all data to 100 Hz, as the sampling frequency changed from 200 to 100 Hz after 2008 (S. Aoi *et al.* 2020). We then rotate the horizontal directions (North–South and East–West) into radial and transverse components using the station-to-epicentre backazimuth for each event-station pair. For large and complex events, such as the 2011 M_{JMA} 9.0 Tohoku-Oki earthquake, the rupture spans several hundred kilometres with multiple asperities (M. Sato *et al.* 2011; M. Simons *et al.* 2011; F. Tajima *et al.* 2013), so a single backazimuth provides only an approximate definition of the radial/transverse directions. Nevertheless, for consistency in the processing across the data set, we derive radial and transverse components for all events, without accounting for finite-fault/source geometry. Fig. 3 shows all the events considered in this study, plotted as a function of epicentral distance and M_{JMA}. Each point represents an event, with colour indicating the corresponding PGA value recorded at the surface station. All available events in the data base for the considered time period were retained, even those with epicentral distances larger than 1000 km.

2.2 Identifying nonlinearity in the frequency domain via computation of resonant frequencies

Nonlinear behaviour induces coseismic velocity changes in the wave propagation medium, which directly affect the resonance frequencies of the material response (D.P. Schaff & G.C. Beroza 2004; J.L. Rubinstein & G.C. Beroza 2004; L.F. Bonilla *et al.* 2019; Y. Lu & Y. Ben-Zion 2022). To track these frequency variations, we need to characterize the site's broad-band response for each recorded event.

We first select the time window where the PGA is identified and the *S*-wave dominates. The duration is magnitude dependent. The radial component at the surface guides the selection of a common time window (t_{win}) for all recorded components (surface and borehole), beginning 1 s before the PGA (Fig. 4a). The same time window is then used in the transverse component (Fig. 4b). The length of the analysed window is defined as follows: 5 s for $M_{JMA} \leq 6$, 10 s for $6 < M_{JMA} \leq 7$ and 15 s for $M_{JMA} > 7$, as suggested by H. Kawase *et al.* (2023).

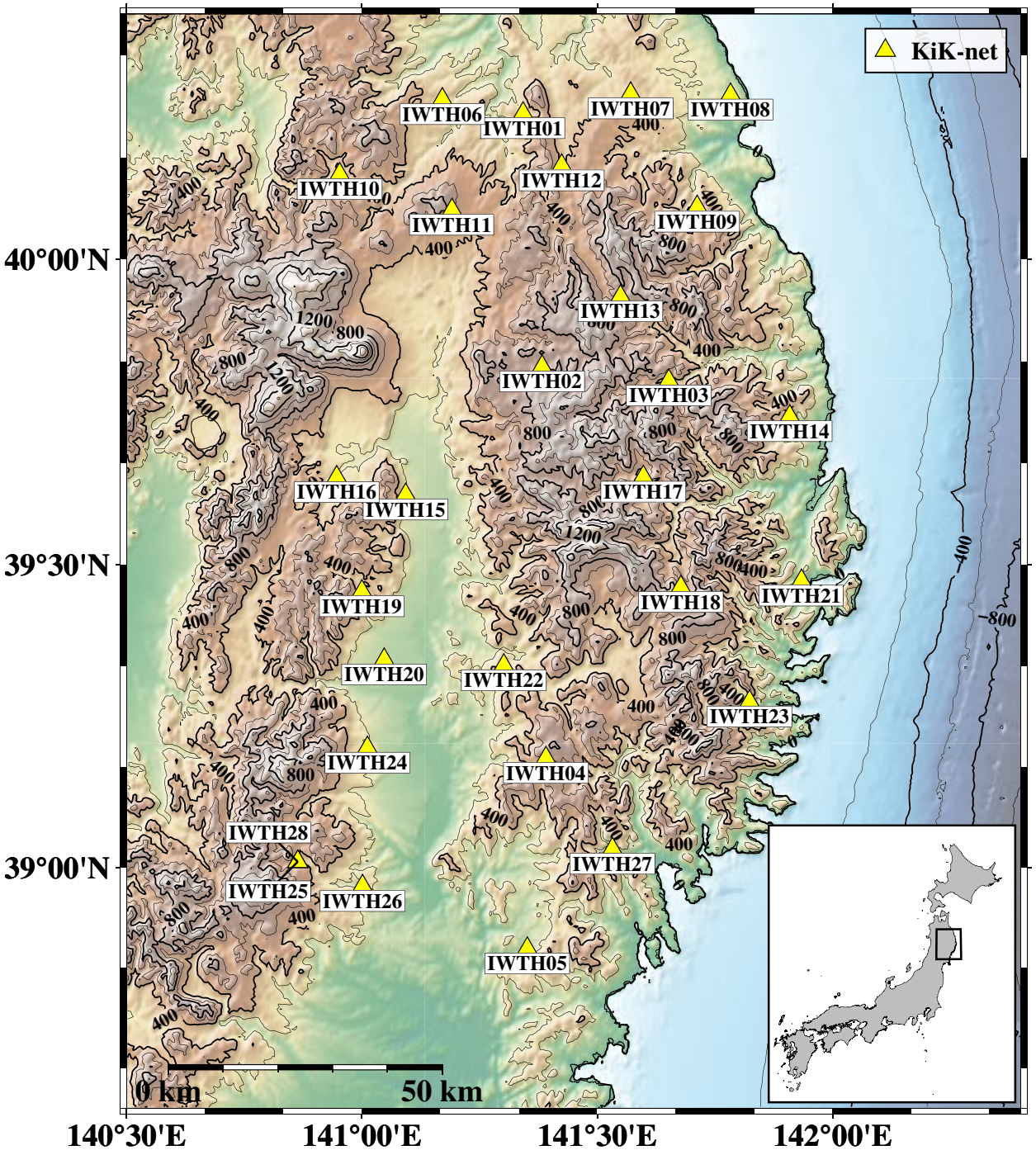

Figure 1. Map of KiK-net stations in Iwate Prefecture. Stations are marked with triangles and labelled with their codes. The inset map at the bottom right shows the location of Iwate Prefecture within Japan.

All time windows are extended to a uniform duration of 20.48 s via zero-padding. This guaranties an equal frequency resolution in the signal processing of the data. From the windowed acceleration records, velocity and displacement are computed following D.M. Boore & J.J. Bommer (2005). In addition, the time derivative of acceleration, called 'jerk', is also calculated. Compared to acceleration, jerk emphasizes higher frequency components, which are more sensitive to abrupt ground motion changes and may reveal additional site-specific information (M. Tong *et al.* 2005).

In this study, we modify the TFRA method originally proposed by S.T. Lai *et al.* (2025b). This method analyses a single component of the ground surface acceleration record to identify broad-band resonance frequencies without the need for a reference site. Its strength lies in this independence, but it lacks the ability to quantify amplification. The original method uses acceleration only. However, in regions having low resonance frequency values, velocity and displacement time-series, which are more responsive to lower frequencies,

Table 1. Characteristics of Iwate KiK-net stations, including station name; predominant resonance frequency ($f_{P,\mathrm{ref}}$) for the transverse component; unimodal (U) or multimodal (M) frequency behaviour; maximum peak ground acceleration recorded at the surface (transverse component); shear-wave velocity at the surface and at the borehole sensor depth; V_{S30}; borehole sensor depth; theoretical vertical shear-wave traveltime down to the borehole depth (tt_{BH}); and classification based on the theoretical vertical shear-wave traveltime down to 100 m depth (tt_{100}), group A ($tt_{100} \leq 0.15$ s) and group B ($tt_{100} > 0.15$ s).

Station	$f_{P,\mathrm{ref}}$ (Hz)	Type	$\mathrm{PGA}_{\mathrm{max},0}$ ($\mathrm{cm\,s^{-2}}$)	$V_{S,0}$ ($\mathrm{m\,s^{-1}}$)	$V_{S,\mathrm{BH}}$ ($\mathrm{m\,s^{-1}}$)	V_{S30} ($\mathrm{m\,s^{-1}}$)	Depth (m)	tt_{BH} (s)	Group tt_{100}
IWTH01	4.75	U	382.04	170	1300	438.04	200	0.26	B
IWTH02	6.60	U	973.53	150	2300	389.57	102	0.12	A
IWTH03	13.11	U	478.45	200	2800	732.56	100	0.07	A
IWTH04	3.42	M	671.26	220	2300	455.93	106	0.11	A
IWTH05	13.24	M	590.59	160	2600	429.20	100	0.11	A
IWTH06	6.23	U	203.17	80	750	431.65	100	0.16	B
IWTH07	6.45	M	214.41	80	2040	395.57	120	0.13	A
IWTH08	2.83	M	345.86	150	2120	304.52	100	0.15	A
IWTH09	16.63	M	515.05	440	2610	966.82	100	0.06	A
IWTH10	13.83	M	123.91	210	1420	496.20	100	0.12	A
IWTH11	2.31	M	125.04	130	1080	343.15	300	0.38	B
IWTH12	3.34	M	748.48	160	1130	367.94	100	0.18	B
IWTH13	19.84	M	331.04	100	2180	620.54	117	0.09	A
IWTH14	10.92	U	493.15	170	2790	816.31	100	0.07	A
IWTH15	6.66	M	331.04	150	680	337.50	122	0.26	B
IWTH16	3.05	M	140.50	260	1160	534.71	150	0.22	B
IWTH17	10.17	M	353.77	240	2960	1269.78	103	0.05	A
IWTH18	15.57	M	434.52	180	2630	891.55	100	0.06	A
IWTH19	7.68	M	360.57	170	1270	482.08	101	0.14	A
IWTH20	6.55	M	382.25	110	430	288.75	156	0.40	B
IWTH21	6.32	M	618.16	150	2460	521.09	100	0.09	A
IWTH22	7.88	M	320.18	190	2780	532.13	100	0.09	A
IWTH23	14.52	U	458.01	370	2200	922.89	103	0.06	A
IWTH24	6.29	M	411.02	180	540	486.41	150	0.29	B
IWTH25	14.21	M	1224.48	430	1810	506.44	260	0.24	A
IWTH26	10.23	U	846.36	130	680	371.06	108	0.20	B
IWTH27	7.49	M	848.69	150	2790	670.31	100	0.07	A
IWTH28	9.85	M	394.94	240	1880	416.75	263	0.29	B

improve frequency identification. To enhance sensitivity to high-frequency components, we also include jerk in the analysis (S.T. Lai *et al.* 2025a). This extended version is hereafter referred to as the stacked sSPSD.

The implemented steps of sSPSD used in this study are as follows. For each selected *S*-wave time window, we compute the Stockwell transform (R. Stockwell *et al.* 1996) of the time-series of jerk, acceleration, velocity and displacement. We used the modulus of the time-frequency representation and normalized its amplitude between 0 and 1 along the time axis. We then stacked, squared and renormalized, yielding a composite time-varying PSD. This reveals the frequencies where energy is concentrated over time.

From the total normalized spectrogram (Fig. 4c), we calculate the median energy as a function of frequency along the time axis. The frequency with the maximum median energy for a given event is identified as the predominant frequency (f_p), shown as red dots in Fig. 4(d). Thus, for each event, we keep both f_p and the corresponding PGA recorded at the surface. A step-by-step illustration of the sSPSD procedure is provided in Fig. A1.

In Figs 5(a) and (d) and 6(a) and (d), the f_p values from all events recorded at stations IWTH14 and IWTH12 are plotted against surface PGA, along with epicentral distance and M_{JMA}.

Material nonlinearity depends on the intensity of the ground motion, which is represented here by the PGA measured at the surface records. To define a baseline for 'linear' site response, we select the PGA range of 1–5 $\mathrm{cm\,s^{-2}}$ as our reference. By averaging a large number of events (with network-wide mean values of 988 and 973 events for the radial and transverse components, respectively, computed across the 28 KiK-net stations), this reference bin yields a stable and statistically robust estimate.

To assess the impact of the ground motion intensity, we compare resonance curves from low (1–5 $\mathrm{cm\,s^{-2}}$) to high (200–400 $\mathrm{cm\,s^{-2}}$) PGA ranges. We group the corresponding events and compute median resonance curves [Figs 5(b) and (e) and 6(b) and (e)]. To improve visual clarity, the resonance curves for the higher PGA bin are smoothed using a Konno-Ohmachi filter (K. Konno & T. Ohmachi 1998) with a bandwidth of 40, due to the limited number of available events. This is not necessary for the reference estimates, given the large number of small amplitude events. For comparison, median SBSR are also shown [Figs 5(c) and (f) and 6(c) and (f)]. Therefore, while the resonance curves in the second rows of Figs 5 and 6 are obtained with only surface data (using sSPSD), the spectral ratios in the third rows are derived from both surface and borehole records (using SBSR). As noted by S.T. Lai *et al.* (2025b), SBSR and sSPSD results show comparable resonance frequency peak features. This agreement is observed for both IWTH14 and IWTH12 (Figs 5 and 6). However, differences between sSPSD and SBSR approaches can arise and mainly affect the overall shape of the resonance curves. This mismatch

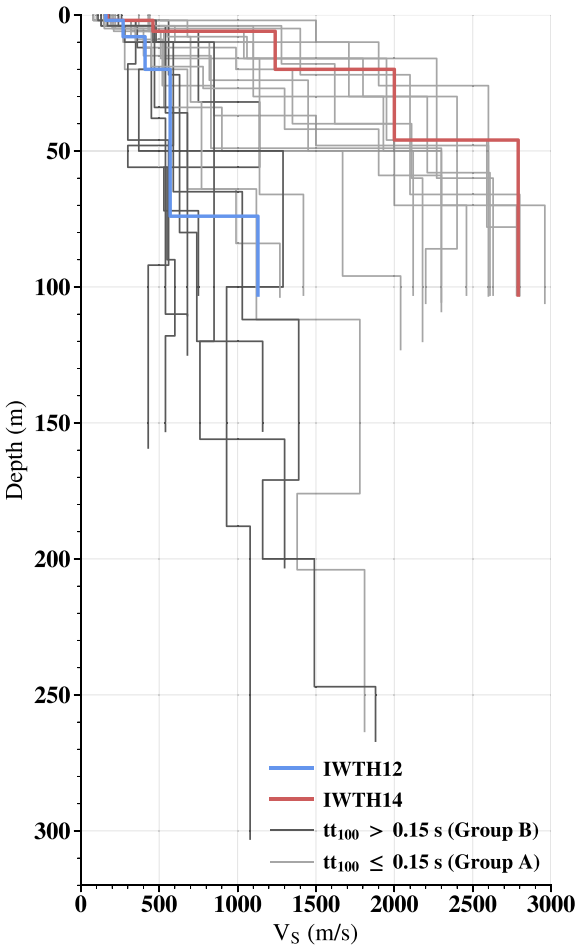

Figure 2. Shear-wave velocity profiles for KiK-net stations in Iwate Prefecture. Stations IWTH12 and IWTH14 are highlighted in blue and red, respectively. Profiles with theoretical vertical shear-wave traveltime down to 100 m depth (tt_{100}) ≤ 0.15 s are shown in grey (group A); all others are shown in black (group B).

may stem from limitations of sSPSD: because it relies exclusively on surface recordings, it contains source and propagation effects, which can influence the spectral estimates. Nevertheless, in both Figs 5 and 6, higher-PGA bins consistently depart from the low-PGA (1–5 cm s^{-2}) trend, showing a shift towards lower frequencies across all panels. Analysis of the median response curves reveals that each station exhibits either a single or multiple resonance peaks. Following the classification by S.T. Lai *et al.* (2025b), we label stations as unimodal (U) if a single dominant peak is present, or multimodal (M) if multiple peaks are observed. Approximately 75 per cent of the stations fall into the multimodal category. Fig. 5 shows an example of unimodal behaviour, while Fig. 6 illustrates a multimodal one. We define the station-specific predominant resonance frequency ($f_{P,\mathrm{ref}}$) as the largest peak in the median curve of the lowest PGA bin. $f_{P,\mathrm{ref}}$ is marked by vertical red dashed lines in Figs 5(b) and (e) and 6(b) and (e), and repeated across all panels in Figs 5 and 6. Note that f_p refers to individual events, while $f_{P,\mathrm{ref}}$ characterizes the overall station response.

Moreover, in Figs 6(b) and (e), the $f_{P,\mathrm{ref}}$ values differ between the radial and transverse components (5.29 and 3.33 Hz, respectively). As noted by S.T. Lai *et al.* (2025b), the differences between the two components involve not only the $f_{P,\mathrm{ref}}$ value but also the overall shape of the resonance curve. These differences may reflect the distinct wavefield content of the two components. Therefore, from this point onwards, we focus on the transverse component, as it better isolates *S*-wave energy, whereas the radial component may include converted *P*-wave contributions. Results from the radial component are provided in the Appendix and referenced when relevant.

Table 1 summarizes these results, which may differ from S.T. Lai *et al.* (2025b) due to our denser data set. The table includes the classification of each station, (U/M), and the corresponding $f_{P,\mathrm{ref}}$ values computed from the transverse component.

Once the broad-band response of each event recorded at each site is determined, we can investigate how resonance patterns evolve with increasing ground motion intensity. Starting from the weak-motion reference range (1–5 cm s^{-2}), we progressively analyse the following intervals: 5–10, 10–25, 25–50, 50–100, 100–200 and 200–400 cm s^{-2}. For each resonance curve, we identify the frequency shift (Δf_P) as the difference between the predominant resonance frequency in the reference bin ($f_{P,\mathrm{ref}}$) and the corresponding peak in the current PGA bin ($f_{P,cur}$). This shift is then normalized by the predominant resonance frequency: $\Delta f_P / f_{P,\mathrm{ref}}$, which allows a proxy of $\Delta v/v$ (S.T. Lai *et al.* 2025b).

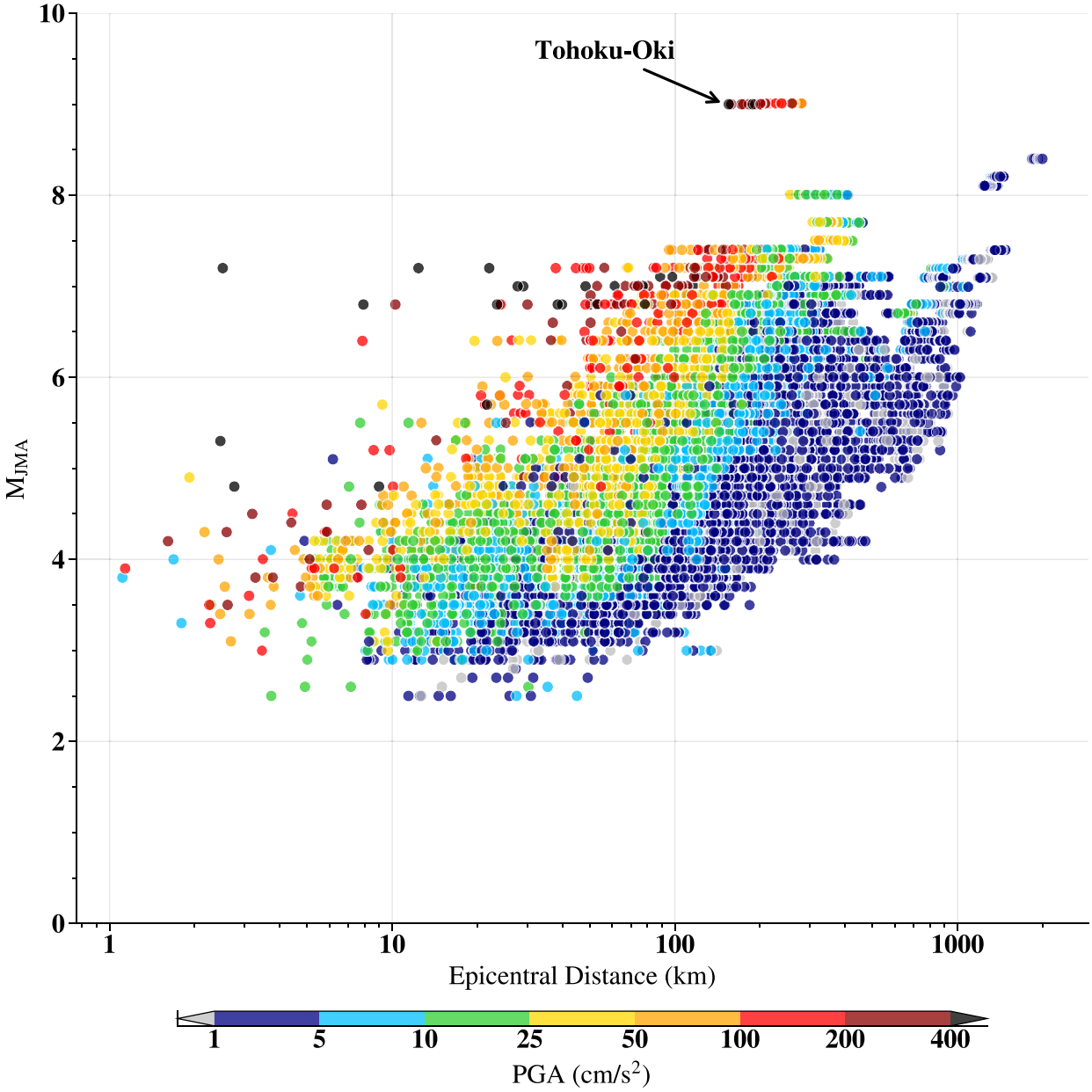

Figure 3. Distribution of PGA as a function of M_{JMA} and epicentral distance, based on data from KiK-net stations in Iwate Prefecture from 2000 to 2022. The colour scale indicates PGA bins.

2.3 Wavelet-based multitaper deconvolution and phase cross-correlation

The conventional method for detecting seismic velocity changes relies on cross-correlation analysis between two records, typically one serving as a reference. Seismic interferometry by deconvolution has proven to be effective in identifying subtle velocity variations (N. Nakata *et al.* 2013; H. Zhang *et al.* 2023). This approach computes the impulse response between two sensors; thus capturing the effects of the soil column on the travel time of various seismic phases (K. Wapenaar *et al.* 2010b; J. Chandra *et al.* 2014).

In the frequency domain, deconvolution is computed by the spectral ratio between the surface and borehole recordings. However, when the denominator of this ratio approaches zero, the division becomes numerically unstable. To address this, we apply a water-level regularization, following K. Wapenaar *et al.* (2010b), using a regularization parameter equal to 10 per cent of the average power spectrum of the borehole wavefield. This approach does not require prior knowledge of the subsurface structure or source characteristics (K. Wapenaar *et al.* 2010a). To improve the robustness of the spectral estimates, we perform the deconvolution using the multitaper method (multitaper deconvolution, MDEC), implemented using the code of G.A. Prieto *et al.* (2009), which reduces bias and variance in spectral estimation (D.J. Thomson 1982).

We also employ the phase cross-correlation (PCC) method (M. Schimmel 1999; S. Ventosa *et al.* 2019), which does not involve multitapering, and neither pre-processing steps such as spectral whitening or bit normalization.

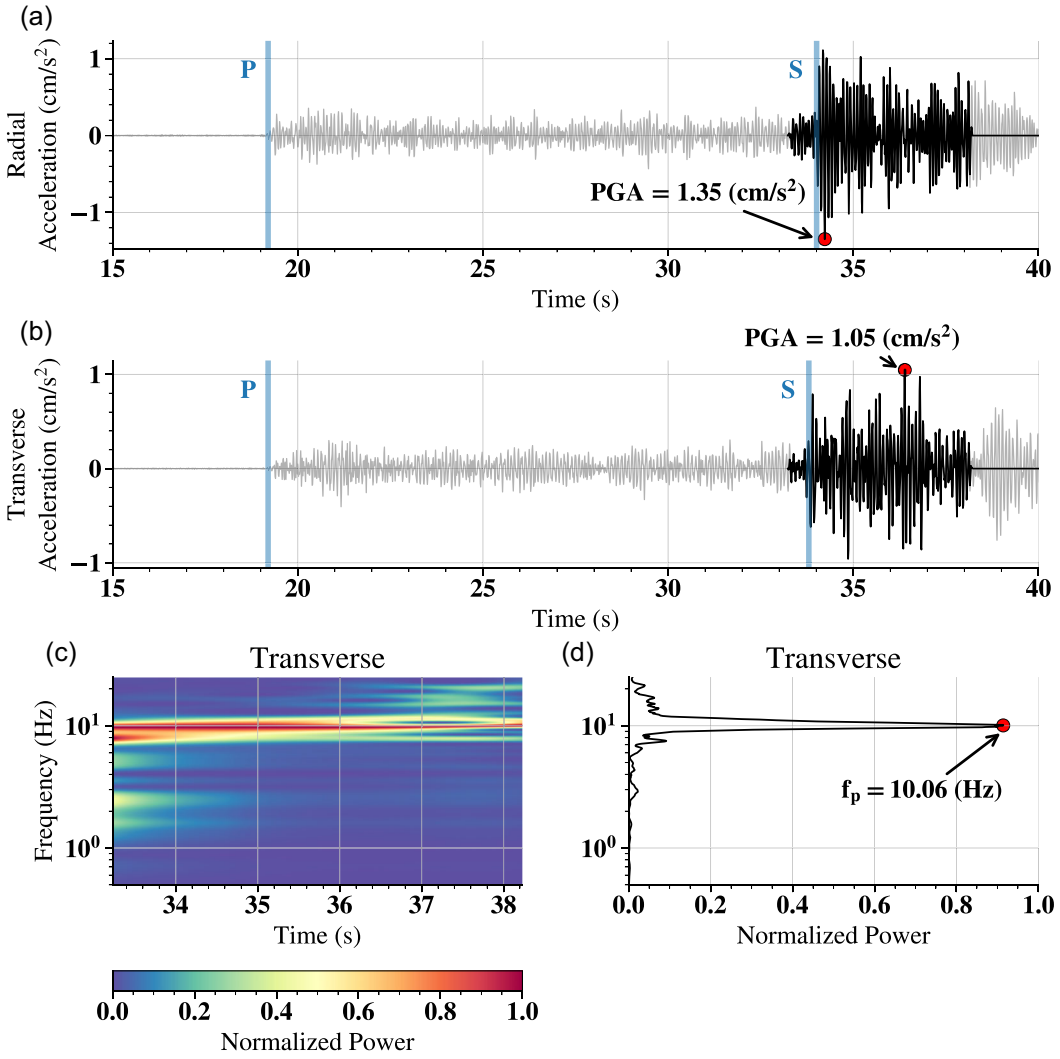

Figure 4. (a) Radial and (b) transverse component of the surface accelerogram recorded at station IWTH14 for the earthquake of 2009 November 30 (M_{JMA} 3.5). The point marks the PGA on each component. *P*- and *S*-wave arrivals are indicated by vertical lines. The dark segment highlights a 5-s time window (starting 1 s before the radial PGA and ending 4 s after it), followed by zero-padding up to 20.48 s (not fully shown). (c) Spectrogram of the full window (20.48 s) obtained using the sSPSD method on the transverse component. (d) Resonance curve computed as the median of the spectrogram using the transverse component; the peak value (point) indicates the event's predominant frequency, f_p.

Hereafter, we refer to the result of MDEC as the interferogram and to that obtained by PCC as the correlogram.

Prior to applying MDEC or PCC, each radial or transverse windowed waveform is decomposed into multiple frequency bands using the continuous wavelet transform (CWT). This enables a detailed time-frequency analysis of the signal. We employ a Morlet wavelet with a central frequency of $f_c = 6$ Hz and use 46 central frequencies ranging from 0.5 to 25 Hz. The lower limit of 0.5 Hz ensures sufficient waveform cycles within the shortest time window of 5 s, while the upper limit of 25 Hz remains below the 30 Hz cutoff of the KiK-net anti-aliasing filter.

The CWT is applied to both surface and borehole records. After decomposition, the inverse continuous wavelet transform (ICWT) is used to reconstruct the signal in the time domain at each central frequency. MDEC and PCC are then performed separately on each wavelet component, using the corresponding borehole signal as the reference. However, in order to have the correct recovery of the impulse response, we need to normalize the ICWT of both surface and borehole by their sum of energies at each frequency band as follows:

$$E_{b,i} = \sum_t \mathrm{ICWT}_{b,i}(t)^2 \tag{1}$$

$$E_{s,i} = \sum_t \mathrm{ICWT}_{s,i}(t)^2 \tag{2}$$

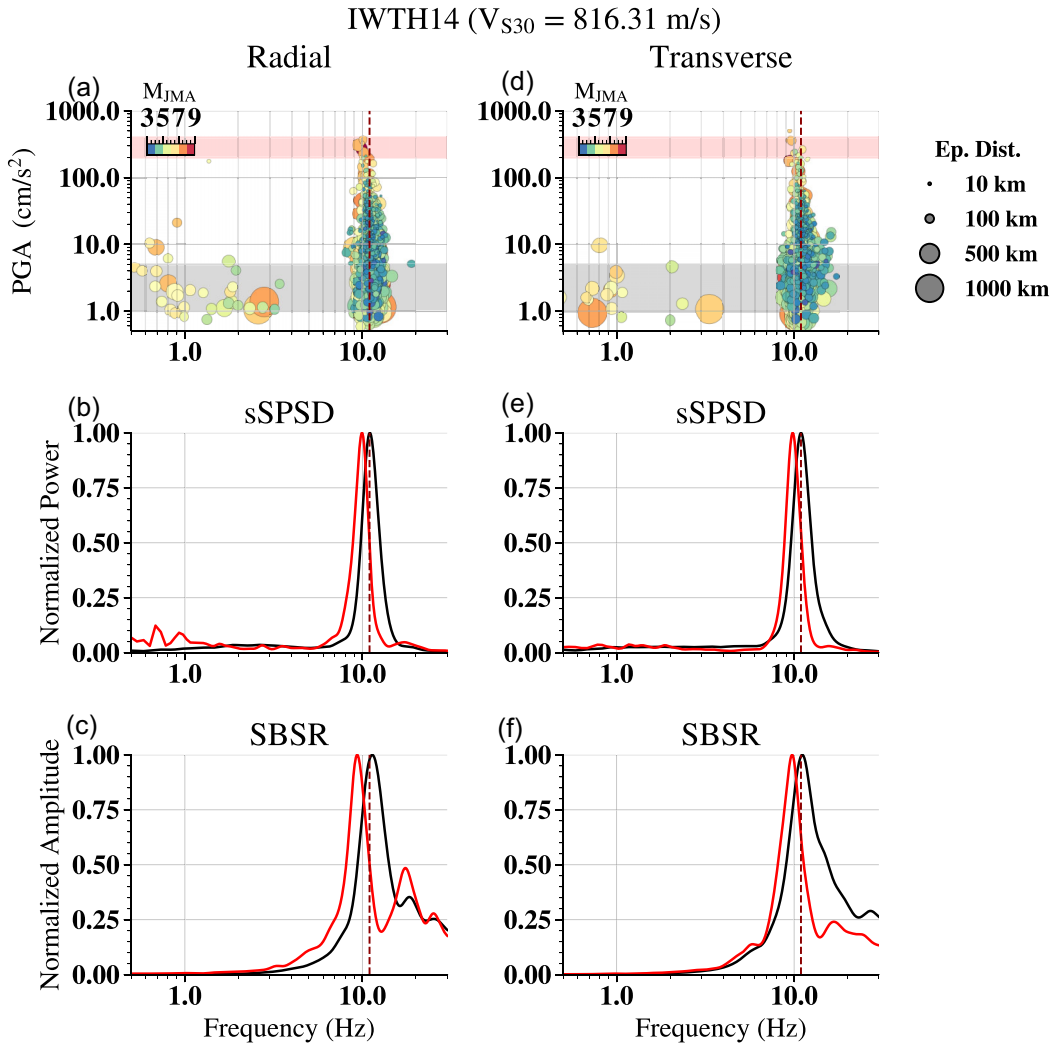

Figure 5. Unimodal station IWTH14 with radial component on the left and transverse component on the right. (a) and (d) show PGA versus predominant frequency (at the surface station). Marker colour indicates the JMA magnitude (M_{JMA}), while marker size reflects the epicentral distance. Grey and red shaded bands highlight events within the 1–5 and 200–400 cm s^{-2} PGA ranges, respectively. For these two PGA ranges, median resonance curves derived from the surface records using sSPSD are shown in (b) and (e), whereas in (c) and (f) are the median surface-to-borehole spectral ratios (SBSR) derived using both surface and borehole records. In all panels, the vertical dashed line indicates the frequency corresponding to the maximum of the median resonance curve for the surface records within the 1–5 cm s^{-2} PGA range.

$$\mathrm{MDEC}(t) = \sum_{i=1}^{I} \mathrm{mdec}_i(t) \cdot (E_{b,i} + E_{s,i}) \tag{3}$$

$$\mathrm{MDEC}_{\mathrm{norm}}(t) = \frac{\mathrm{MDEC}(t)}{\sum_{i=1}^{I}(E_{b,i} + E_{s,i})}. \tag{4}$$

Eqs (1) and (2) define the energy of the reconstructed wavelet components at the borehole ($E_{b,i}$) and surface ($E_{s,i}$), respectively. The energy for each frequency band i is computed as the sum of the squared amplitude of the inverted signal at a given frequency band. In eq. (3), each individual contribution $\mathrm{mdec}_i(t)$ (shown here for MDEC; the equivalent for PCC is $pcc_i(t)$) is weighted by the sum of the borehole and surface energy values, $(E_{b,i} + E_{s,i})$. Finally, eq. (4) normalizes the result by the total energy across all frequency bands. Further details on the effect of energy normalization can be found in eqs (A1), (A2), and Fig. A2. In Figs 7(a) and (b), the grey curves represent the resulted deconvolved and correlated signals for events between 1 to 5 cm s^{-2} at station IWTH14. The obtained impulse response is then normalized by removing its mean and dividing by its standard deviation in Figs 7(a) and (b) to show the stability of individual computations (in grey) and the mean (in red).

To enhance the signal-to-noise ratio, we stack all individual computations separately for each PGA bin. The stacking process is performed in two steps: initially, a linear stack is applied to groups of 15 events selected in chronological order. Then, a time scale phase-weighted stack [ts-PWS; S. Ventosa *et al.* (2017)] is performed on these linear stacks (Figs 7a and b). This technique utilizes

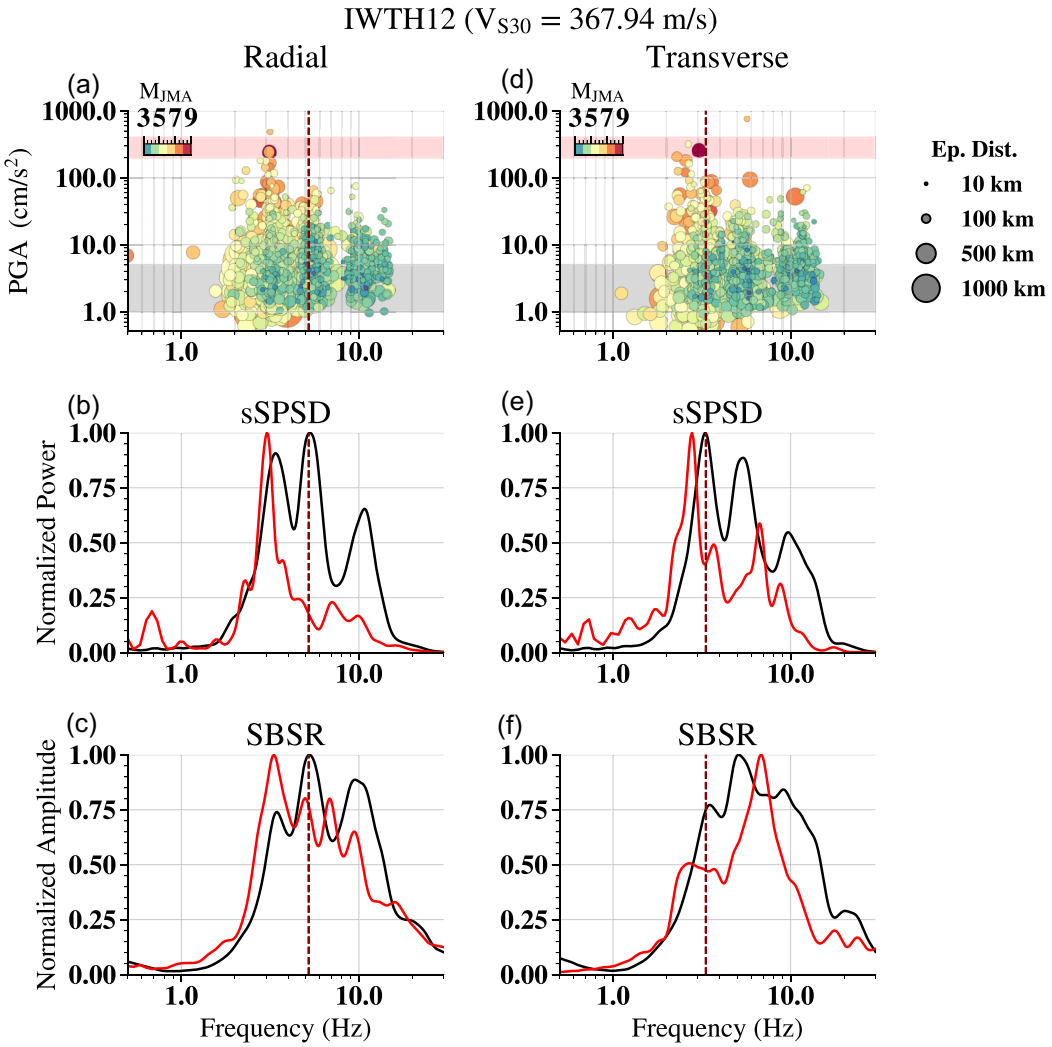

Figure 6. Multimodal station IWTH12 with radial component on the left and transverse component on the right. (a) and (d) show PGA versus predominant frequency (at the surface station). Marker colour indicates the JMA magnitude (M_{JMA}), while marker size reflects the epicentral distance. Grey and red shaded bands highlight events within the 1–5 and 200–400 cm s^{-2} PGA ranges, respectively. For these two PGA ranges, median resonance curves derived from the surface records using sSPSD are shown in (b) and (e), whereas in (c) and (f) are the median surface-to-borehole spectral ratios (SBSR) derived using both surface and borehole records. In all panels, the vertical dashed line indicates the frequency corresponding to the maximum of the median resonance curve for the surface records within the 1-5 cm s^{-2} PGA range.

phase information to weight the stacking process, thereby enhancing signal coherence in regions with higher energy content (Figs 7c and d), while attenuating less coherent portions of the linear stacks in both the time and frequency domains. To illustrate the temporal weighting applied during the time scale phase-weighted stack, Figs 7(c) and (d) show, as a dashed blue curve, the envelope computed by taking the maximum amplitude across all frequencies at each time-step from the phase-weighted spectrogram. This envelope highlights the time intervals where the signal is most coherent across events (around 0.16 s).

After stacking, we upsample the signal, which is originally sampled at 0.01 s, by a factor of 10 to improve the temporal resolution of the cross-correlation fit during the stretching analysis (Section 2.4).

2.4 Computing velocity changes: the stretching method

To compare the signals obtained from stacking, we apply the stretching method introduced by O.I. Lobkis & R.L. Weaver (2003), using the Python code provided by L. Viens *et al.* (2018). This technique requires a reference signal, which in our case is the stacked curve corresponding to the 1–5 cm s^{-2} PGA bin. The other stacked curves are compared with this reference [black and blue curves in Fig. 8(a)]. The method is based on the principle that a change in arrival time, such as that observed in Fig. 8(a), is directly related to a change in seismic velocity. This relationship is quantified by the stretching factor (ε), calculated as:

$$dt/t = -dv/v = \varepsilon.$$

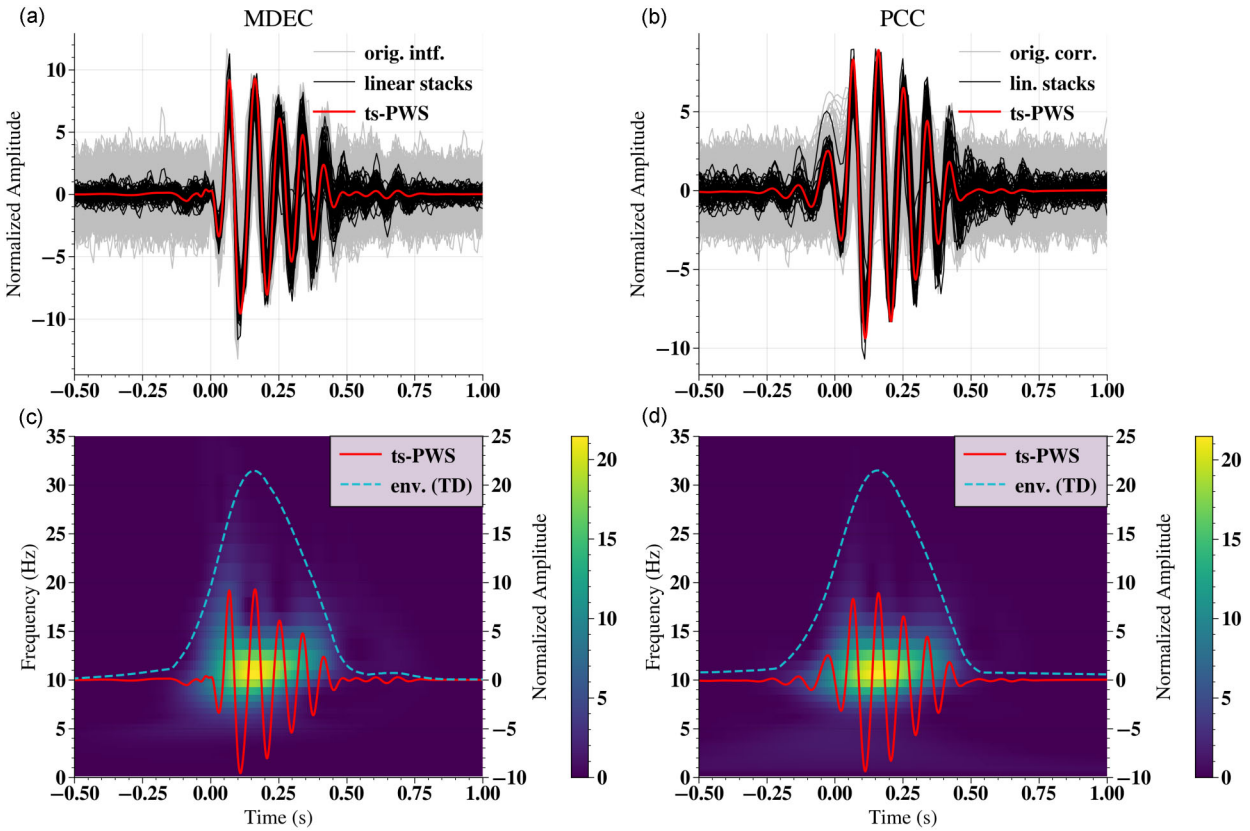

Figure 7. Computed interferogram using the MDEC method (a) and correlogram obtained using PCC method (b) between the borehole (reference) and the surface computed using transverse component data recorded at the station IWTH14 within PGA 1 to 5 cm s^{-2}. The individual interferograms/correlograms are shown in grey, the linear stacks of every 15 interferograms/correlograms are shown in black, and the timescale phase-weighted stack (ts-PWS) is shown in red. (c) and (d) show the ts-PWS (red line), its spectrogram (colourmap) and its envelope (dashed blue line), for MDEC and PCC methods, respectively.

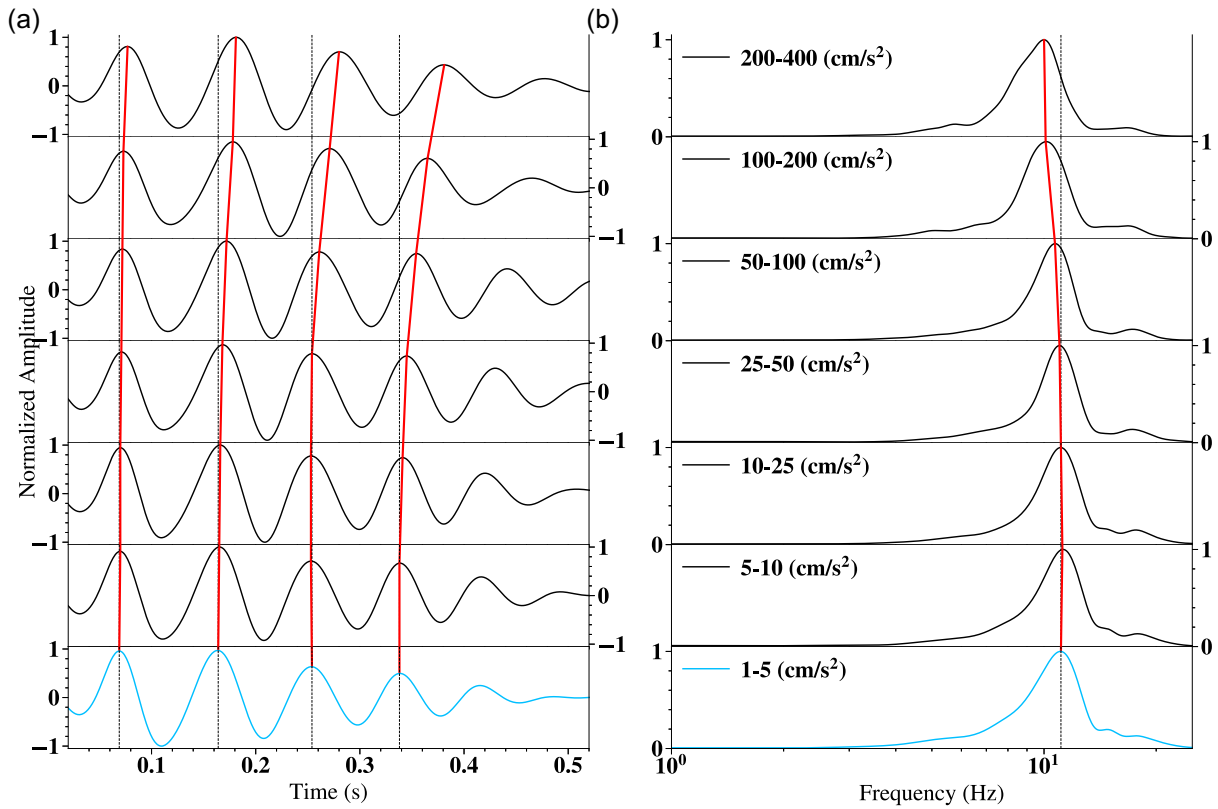

Figure 8. Interferograms computed using the MDEC technique on the transverse component data of IWTH14 station. Each subplot shows the ts-PWS interferogram for a PGA bin (a) and the corresponding amplitude spectrum (b). The reference curves are shown in blue, while the red lines connect the peak positions in time (a) and frequency (b).

The stretching method assumes that a homogeneous velocity perturbation occurs within the medium over a defined time interval; in this paper, 0.5 s around the theoretical vertical shear-wave traveltime down to the borehole (tt_{BH}).

3 RESULTS

3.1 Evidence of nonlinear site response from traveltime delays and frequency shifts

During strong ground shaking, the incident wavefield can induce nonlinear behaviour in near-surface materials, altering their elastic properties, and consequently, seismic wave velocities. The extent of this effect depends on both the material properties and the amplitude of the incoming ground motion. Using the vertical array configuration of KiK-net stations, we investigate how increasing ground motion intensity affects shear-wave traveltimes between surface and borehole sensors.

A clear manifestation of this effect is the progressive delay in the arrival times of seismic waves with increasing ground motion intensity. This is illustrated in Fig. 8(a) for station IWTH14, where the stacked interferograms corresponding to the reference PGA bin (1–5 cm s^{-2}) are compared with those of higher PGA bins (5–10, 10–25, 25–50, 50–100, 100–200 and 200–400 cm s^{-2}). The delay becomes more pronounced as the PGA increases, as well as the cumulative shift in arrival time indicating a reduction in shear-wave velocity. This effect is further supported by the Fourier transforms of the interferograms (Fig. 8b), which reveal a systematic shift of the resonance frequency toward lower values with increasing shaking intensity. These observations indicate material nonlinearity, detectable through the velocity variations of the medium.

While this type of analysis requires colocated surface and borehole sensors, an expensive and less common setup, the ability to detect such nonlinear behaviour using only surface data is highly valuable. The method presented in this study, sSPSD, offers a practical means of identifying site resonance frequency and its changes without relying on borehole instrumentation.

Notably, the resonance frequencies observed in Fig. 8(b) for the lowest (1–5 cm s^{-2}) and highest (200–400 cm s^{-2}) PGA bins, obtained from the Fourier analysis of MDEC, match those derived from sSPSD and SBSR in Figs 5(e,f), respectively. Moreover, in Fig. A3, the sSPSD and the Fourier analyses of MDEC and PCC reveal comparable resonance peaks.

This consistency across surface-only (sSPSD) and borehole-based (MDEC, PCC, SBSR) approaches supports the reliability of the resonance-frequency estimates obtained with sSPSD, despite the presence of source and path effects. These results suggest that site effects dominate the ground motion, at least in this data set.

While this agreement is evident for unimodal stations, the situation becomes more complex at multimodal sites, where a single peak cannot capture the full nonlinear behaviour. For this reason, we evaluate the velocity change in the time domain, which works for both unimodal and multimodal sites.

3.2 Consistency between MDEC and PCC methods

Both the time delay and the frequency shift, observed in Fig. 8, suggest underlying changes in the propagation velocity of the waves. The stretching method provides a quantitative estimate of this variation, expressed as a relative velocity change ($\Delta v/v$) for each PGA bin. Fig. 9(a) shows the velocity change results obtained from both MDEC and PCC methods in the transverse component, for all stations. As shown in Fig. 9(a), the results from the two methods are consistent. Fig. 9(b) displays the average number of events per station for each PGA bin. The results for the radial component are provided in Fig. A4. Fig. 9(b) illustrates that the number of available events decreases with increasing PGA. Note that bins with fewer than two events (events <2) were excluded from this and all subsequent analyses, so that that each stack reflects stable trends rather than being biased by a single event.

Before applying the stretching method, we perform a normalized cross-correlation (NCC) between the reference and the analysed interferograms or correlograms. The analysis window is centered around tt_{BH}, spanning from $tt_{BH} - 0.05$ to $tt_{BH} + 0.45$ s. We then extract the maximum cross-correlation coefficient (NCC_{MAX}) and the corresponding time lag (t_{lag}). Only interferograms/correlograms that meet the criteria $NCC_{MAX} \geq 0.85$ and $t_{lag} \leq 0.05$ s (10 per cent of the window length) are retained. This selection warrants that only highly coherent and time-aligned signals are included in the stretching analysis, thereby minimizing unreliable estimates. More details on this quality control procedure are provided in Fig. A5. This preprocessing is needed because material nonlinearity does not have a constant velocity change in time. Earthquake strong ground motion can have different amplitudes and durations, making the velocity changes vary in time. As a result, the stretching method needs to be used with caution and we need to develop better signal processing techniques to track these non-stationary velocity changes during strong shaking.

Given the strong agreement between MDEC and PCC methods, in the following sections, we present only the $\Delta v/v$ results obtained from the MDEC method applied to the transverse component.

It is worth mentioning that the PCC technique is one order of magnitude faster than the MDEC method, as MDEC computes the multitaper spectral estimation prior to the deconvolution. This is important when analysing a large earthquake database. The fact that both methods give similar results is encouraging for the use of the PCC technique in future studies.

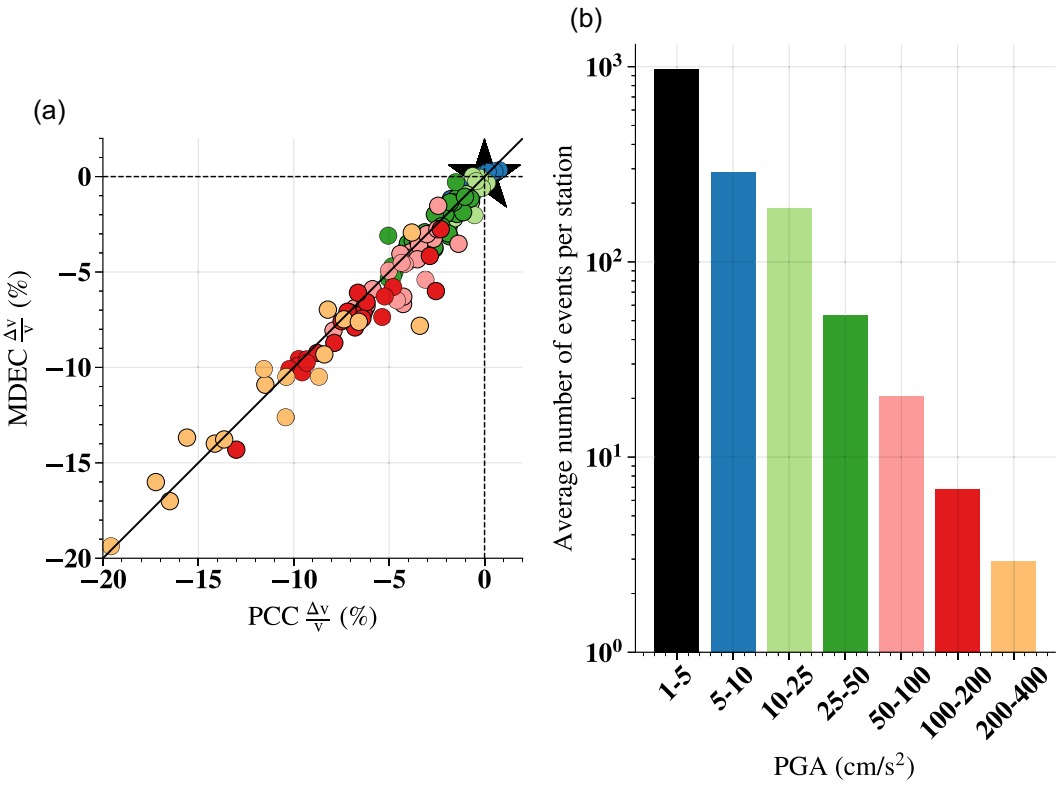

Figure 9. (a) Velocity changes computed with MDEC versus PCC methods using the transverse component for all stations in Iwate Prefecture. For each station and each PGA bin larger than 5 cm s^{-2}, velocity change is represented by a dot. The big black star represents the reference PGA bin (1–5 cm s^{-2}). The 1:1 line is represented in black. (b) Average number of events per station for each bin of PGA. For (a) and (b) colours correspond to the PGA bin.

3.3 PGA amplitude-dependent velocity variations

In previous sections, we have seen that the velocity of the propagation medium decreases as the PGA of the incoming motion becomes larger. Concomitantly, there is a reduction in the resonance frequency of the sediments. Quantifying the velocity changes during strong motion is important because this gives information about the nonlinear behaviour of the material. The relation between these seismological observations and earthquake engineering needs is through the reduction of the shear modulus (B.O. Hardin & V.P. Drnevich 1972; K. Ishihara 1996). Since the shear modulus, μ, is proportional to the square of the shear-wave velocity, and the velocity change is $\Delta v/v_0 = v/v_0 - 1$, we can then write $\mu/\mu_0 \sim (1 + \Delta v/v_0)^2$ (L.F. Bonilla *et al.* 2019), where $\Delta v = v - v_0$, v is the perturbed velocity, and v_0 is the initial velocity. Note that the simplified notation $\Delta v/v$ is used throughout the text (including earlier sections) to denote $\Delta v/v_0$.

Fig. 10(a) shows the distribution of velocity changes for each bin, with stations grouped according to tt_{100} on the transverse components. The boxes display the median and interquartile range for each group. Individual site-specific responses are not preserved. The velocity changes are those computed using the stretching method applied to stacked interferograms. The variability between sites remains evident from the spread of values within each group. Moreover, the dispersion in $\Delta v/v$ also appears to increase at higher PGA levels. Despite this variability, a general trend of increasing $\Delta v/v$ magnitude with PGA is clearly observed.

Fig. 10(b) presents the frequency shifts, $\Delta f_P/f_{P,\mathrm{ref}}$, calculated from the stacked sSPSD. Velocity and frequency changes exhibit comparable trends in terms of magnitude and PGA dependence, although $\Delta f_P/f_{P,\mathrm{ref}}$ tends to be larger. On average, 2.5 per cent higher over the entire PGA bin distribution. This difference is due to the higher sensitivity of the sSPSD method to the shallow interfaces, where nonlinear effects are concentrated (J.L. Rubinstein & G.C. Beroza 2005). Moreover, in the case of $\Delta v/v$, the two profile families show different behaviour, with group A ($tt_{100} \leq 0.15$ s) generally showing larger velocity changes. In contrast, the $\Delta f_P/f_{P,\mathrm{ref}}$ measurements show an opposite trend, with group B ($tt_{100} > 0.15$ s) tending to exhibit larger frequency changes. The results for the radial component, which exhibits similar patterns as those for the transverse direction, are shown in Fig. A6. The opposite trends observed between the two groups in velocity and frequency responses reflect the different physical sensitivities of the techniques used to estimate $\Delta v/v$ and $\Delta f_P/f_{P,\mathrm{ref}}$, together with differences in borehole depth and velocity structure between groups A and B (see Fig. 2 and Table 1). These aspects are discussed in more detail in Section 4.

In addition to the two-family classification based on the tt_{100}, we explore whether the relative velocity changes correlate with V_{S30}. Fig. 11 displays the relative velocity changes plotted against V_{S30}, with each colour representing a different PGA bin. Similarly to Fig. 10(a), higher PGA bins tend to be associated with larger velocity variations. In addition, this increase is shown to be almost the

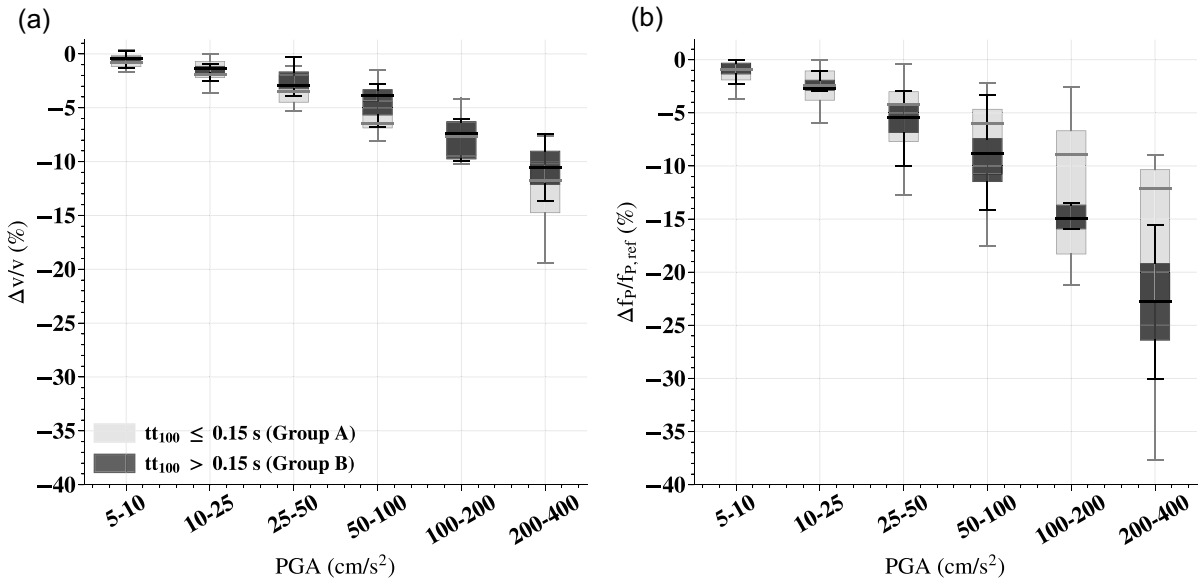

Figure 10. For each PGA bin, (a) shows velocity changes obtained using the stretching method on the transverse component of stacked interferograms, and (b) shows frequency changes obtained from the f_P shift between the median resonance curves. Both (a) and (b) measure the velocity/frequency changes with respect to the reference 1–5 cm s^{-2} PGA bin (not shown in the plots). The grey and black boxes indicate the interquartile ranges, with the lines inside representing the medians: grey for group A ($tt_{100} \leq 0.15$ s) and black for group B ($tt_{100} > 0.15$ s). The whiskers extend to the most extreme data points within 1.5 times the interquartile range.

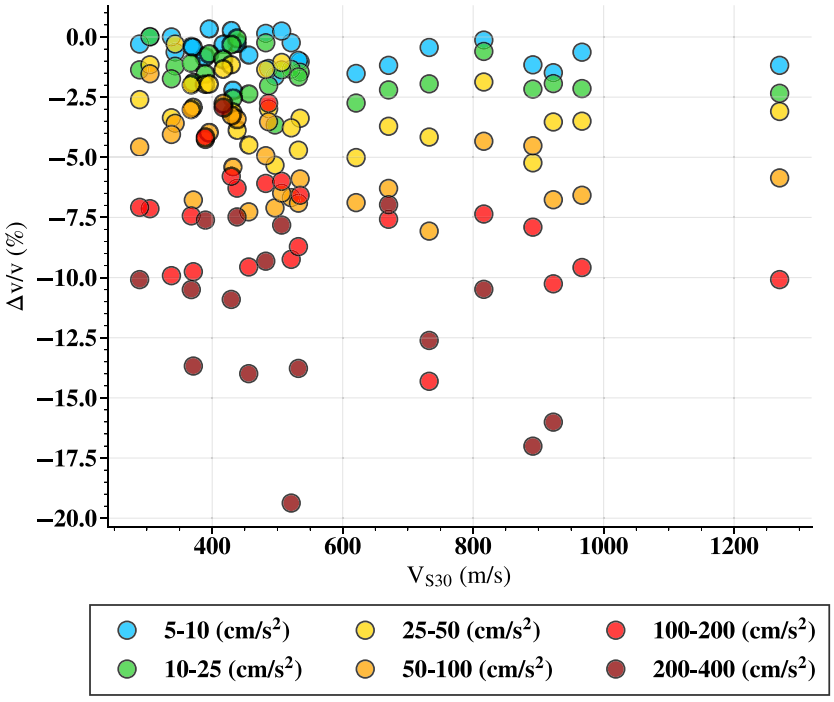

Figure 11. Velocity changes estimated using the stretching method applied to transverse component stacked interferograms plotted against the V_{S30} values of each site. Results are grouped by PGA bins.

same regardless of the V_{S30} value. However, at higher PGA bins, a large variability is observed within the same PGA range as is also shown by Fig. 10(a). Therefore, V_{S30} is not a good proxy to predict nonlinear site response.

The resulting shear modulus variations as a function of PGA at all stations are shown in Fig. 12(a). For PGA in the range of 200–400 cm s^{-2}, the median response shows a reduction in stiffness, with the shear modulus reaching, on average, approximately 80 per cent of its initial value.

Fig. 12(a) also includes a comparison of our μ/μ_0 results, which are specific to Iwate Prefecture and derived from velocity variations, with those of S.T. Lai *et al.* (2025b), who report average shear modulus reductions for the whole of Japan derived from frequency shifts using $\mu/\mu_0 \sim (1 + \Delta f_P/f_{P,\mathrm{ref}})^2$. The shear modulus reductions obtained from the two approaches exhibit a consistent overall

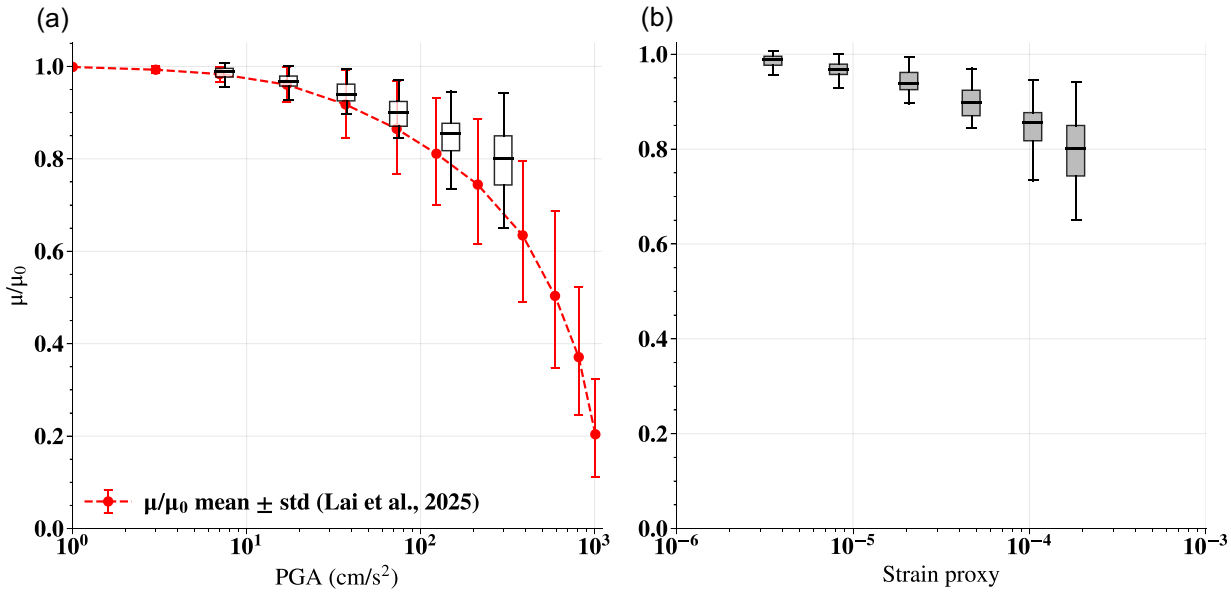

Figure 12. Normalized shear modulus as a function of (a) PGA and (b) strain proxy (PGV_{med}/V_{S30}). The boxes represent the interquartile range, the horizontal lines within them are the medians and the whiskers extend to the most extreme data points within 1.5 times the interquartile range. In (a), the dots and dashed line indicate the mean μ/μ_0 values reported by S.T. Lai *et al.* (2025b) for all Japan, and the vertical error bars represent ± 1 standard deviation to illustrate data variability.

trend, although the results of S.T. Lai *et al.* (2025b) extend to larger PGA values. The small amplitude difference between the two studies (less than 5 per cent on average across the common PGA bins) reflects the combined effects of different spatial coverage and the distinct physical sensitivities of μ/μ_0 inferred from velocity variations and from frequency shifts. Indeed, as discussed above, the sSPSD method is more sensitive to shallow interfaces, where nonlinear behaviour is concentrated.

To account for the level of dynamic strain, we also evaluate the use of peak ground velocity (PGV) within the PGV/V_{S30} proxy proposed by I. Idriss (2011), which has been widely used as a physically meaningful indicator of near-surface strain (R. Takagi & T. Okada 2012; K. Sawazaki & R. Snieder 2013). The transverse accelerograms are integrated following D.M. Boore & J.J. Bommer (2005) to obtain the velocity time series, from which the PGV is calculated. For each station, the PGV measurements are grouped according to the previously defined PGA bins. Within each bin, the median PGV, PGV_{med}, is calculated. These values are then used to estimate strain as PGV_{med}/V_{S30} and are plotted against μ/μ_0 in Fig. 12(b).

4 DISCUSSION

Using KiK-net data from 28 surface-borehole pairs in Iwate Prefecture, we investigate site response through velocity and frequency variations as a function of increasing PGA recorded at surface stations.

We modify the original time-frequency resonance analysis (S.T. Lai *et al.* 2025b) by stacking displacement, velocity, acceleration and jerk in the time–frequency domain, therefore improving the broad-band resonance frequency identification. The resulting method is referred to as the stacked sSPSD. This improvement enables a more accurate resolution of resonance patterns excited by both shallow and deep geological structures.

The identification of the pair PGA and resonance frequency helps visualize how distant and high-M_{JMA} events tend to excite lower frequency components, while close low-M_{JMA} events typically generate broader and higher-frequency energy, which predominantly activates the shallower soil layers, as represented in Figs 5 and 6(a) and (d).

Furthermore, the resonance curves show a generally consistent trend with the SBSR, as also observed by S.T. Lai *et al.* (2025b), although some differences appear.

However, the identification of resonance frequencies becomes difficult at sites where the response has multiple peaks. In such cases, isolating a single frequency is not straightforward and may introduce errors when computing frequency shifts and the related velocity changes. Visualizing the broad-band response and earthquake effects at the site allows nonlinear site effects to be directly related to shallow and deep structures. Interestingly, those sites having a resonance at high frequencies and consequently classified as stiff material (i.e. IWTH14) still show a clear nonlinear signature. This is explained by the presence of shallow thin layers that respond nonlinearly in case of strong motion. In addition, these sites overlay rock material, producing a strong impedance contrast, which amplifies the incident wavefield. This also explains why V_{S30} is not sensitive to nonlinear behaviour: as an averaged parameter, it masks

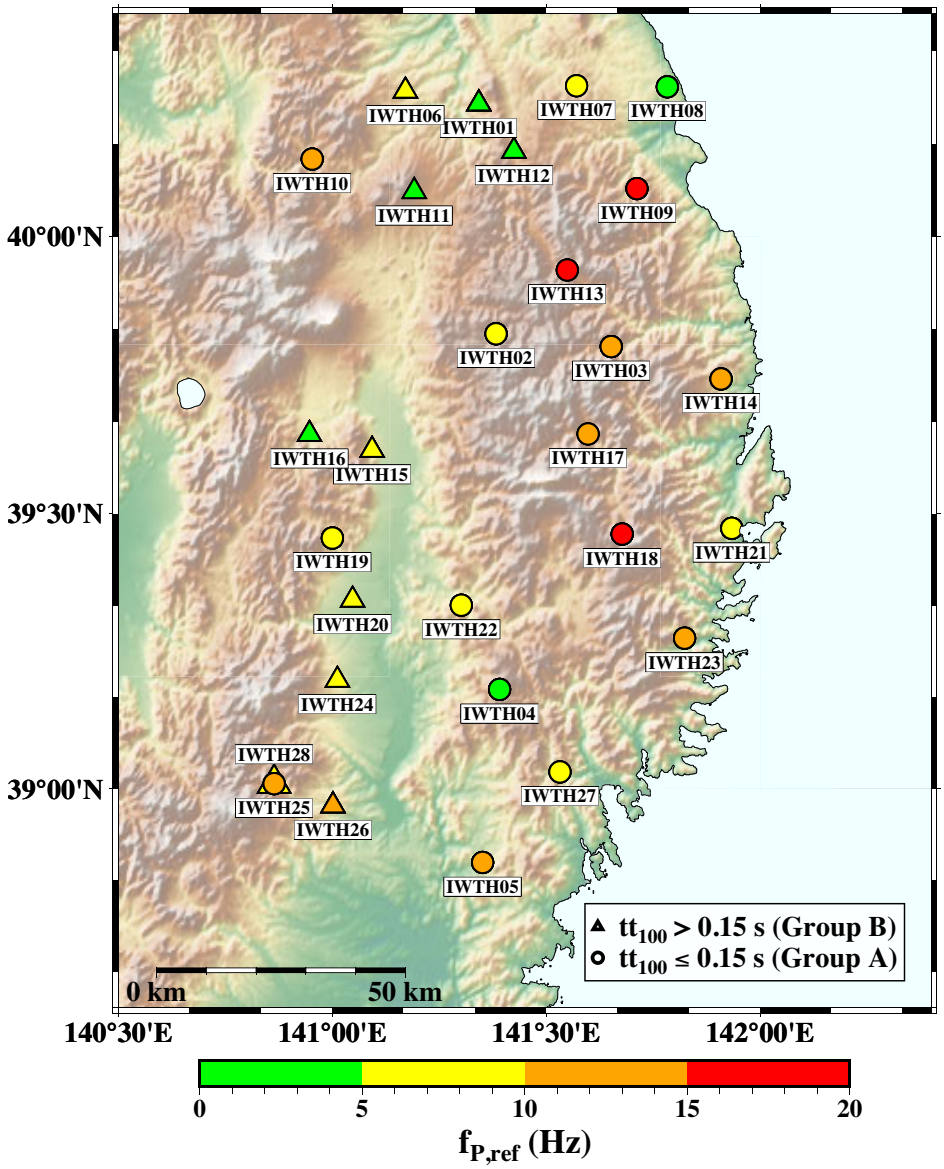

Figure 13. Map showing the $f_{P,\mathrm{ref}}$ distribution for the transverse component. The $f_{P,\mathrm{ref}}$ values are grouped into four classes: $f_{P,\mathrm{ref}} \leq 5$ Hz, $5 < f_{P,\mathrm{ref}} \leq 10$ Hz, $10 < f_{P,\mathrm{ref}} \leq 15$ Hz and $f_{P,\mathrm{ref}} > 15$ Hz. Stations of group A ($tt_{100} \leq 0.15$ s) are indicated with a circle, while stations of group B ($tt_{100} > 0.15$ s) are indicated with a triangle.

the presence of low-velocity layers. These findings are consistent with Y.P. Dhakal *et al.* (2025), who also reported that the degree of nonlinearity does not systematically correlate with V_{S30}.

This interpretation is further supported by the spatial distribution of $f_{P,\mathrm{ref}}$ values (Fig. 13). Stations with short tt_{100} (group A), mainly in the eastern mountain ranges, systematically exhibit high $f_{P,\mathrm{ref}}$, reflecting the presence of thin soft layers over rock. Such conditions are known to amplify ground motion and may favour nonlinear behaviour in the shallow subsurface (C. Gélis & L.F. Bonilla 2012). By contrast, stations in the central valley and northern foothills, are characterized by thicker sedimentary deposits, resulting in longer tt_{100} (group B) and lower $f_{P,\mathrm{ref}}$. Few exceptions arise at multimodal sites, where identifying a single frequency peak is not representative of the overall subsurface behaviour.

Using KiK-net configuration, namely the presence of sensors at the ground surface and depth, it is possible to isolate the effect of the earthquake shaking on the soil column. In this study, we use the MDEC and PCC. We show that both techniques produce comparable results, and PCC has a computational cost of one order of magnitude lower than MDEC, making it a practical alternative for large-scale applications. When comparing frequency and time domain techniques, sSPSD, PCC and MDEC, respectively, we see a close agreement and all are complementary.

However, when velocity and frequency changes are compared across different sites (i.e. groups A and B), contrasting behaviours emerge, as illustrated in Fig. 10. Stations in group B are characterized by thicker near-surface low-velocity layers than those in group A

and are therefore expected to experience larger strain levels for comparable ground motion amplitudes, leading to stronger nonlinear effects (I.A. Beresnev & K.L. Wen 1996). This behaviour is consistently captured by the frequency changes derived from sSPSD, whereas the velocity changes exhibit an opposite trend.

This difference primarily reflects the distinct physical sensitivities of the methods. The sSPSD approach relies exclusively on surface recordings and therefore captures the response of the shallowest layers, where nonlinear effects are concentrated (J.L. Rubinstein & G.C. Beroza 2005). In contrast, velocity changes derived from MDEC and PCC, which use a borehole reference, represent an average velocity perturbation along the propagation path between the surface and borehole sensors and thus depend on both borehole depth (generally larger for group B) and the velocity structure sampled along this path. As a result, $\Delta v/v$ should be interpreted as a relative measure of medium perturbation between the surface and borehole sensors.

In the case of complex frequency responses (i.e. multimodal sites), time-domain analyses based on broad-band interferograms (or correlograms) capture the overall effect of the entire soil column, making it possible to detect the relative velocity changes of the whole medium. In contrast, frequency-domain approaches track one or several resonance frequencies that are representative of a limited set of layers close to the surface. We need to pursue the research of these methods to eventually identify the layers affected by nonlinearity.

5 CONCLUSIONS

Drawing on more than two decades of KiK-net observations, our results show that both the onset and intensity of nonlinear site response are strongly site dependent. This is evident in the substantial variability of velocity and frequency changes across stations exposed to comparable shaking levels. Such variability highlights the limitations of applying uniform thresholds and calls into question the traditional reliance on V_{S30} in ground-motion models.

Consistent results emerge from surface-borehole time-domain analyses. The results of these approaches, however, rely on borehole depth and subsurface velocity structure, which vary from site to site. As a result, the inferred $\Delta v/v$ represents a relative measure of medium V_S perturbation. Despite this, the approaches effectively capture broad-band velocity changes, including at complex (i.e. multimodal) sites.

On the other hand, the computation of average resonance curves for different intensities of the ground motion allows frequency shifts and attenuation to be easily tracked. Because this approach does not rely on borehole references, it can be applied to many seismic networks worldwide. Furthermore, this method is sensitive to the shallowest layers. As a result, it highlights larger frequency shifts at sites with thick near-surface low-velocity sediments, where nonlinear behaviour is expected to be strongest. However, as a surface-based approach, the average resonance curve may be affected by source and propagation effects, while its quality depends on the amount of data available. Sites having a complex response (i.e. multimodal) still remain a challenge. These results, however, suggest that site effects dominate the ground motion in these data.

In summary, velocity changes and frequency changes provide complementary perspectives, and their combined use, where feasible, enhances the reliability of nonlinear site-response detection. These findings suggest important implications for seismic hazard assessment, particularly in highlighting the potential for site-specific effects during strong shaking. At the same time, key uncertainties remain regarding the relative contribution of different soil layers within the soil column to nonlinear processes, and how these are governed by mechanisms such as material degradation and pore-pressure changes. Progress in this direction will depend on detailed studies at a limited number of well-instrumented sites, especially vertical arrays with pore-pressure transducers, which can offer the critical observations needed to refine our understanding and modelling of these phenomena.

ACKNOWLEDGMENTS

We acknowledge the financial support of the ANR project E-CITY, grant number ANR-21-CE22-0020. We also thank the National Research Institute for Earth Science and Disaster Resilience (NIED), Japan, for providing access to the KiK-net recordings and site data, which greatly facilitated this study. We thank Editor Dr Anne Obermann, Assistant Editor Fern Storey and the anonymous reviewers for their constructive and insightful comments, which improved the manuscript. We are grateful for valuable discussions with Céline Gélis, Etienne Bertrand, Karina Loviknes, and José Ignacio Bustos Fonseca, which were highly beneficial to our work.

AUTHOR CONTRIBUTION

This work is part of the Ph.D. research of AS, who contributed to the code development, performed the data processing, analysed the results and wrote the paper. LFB conceived the project and developed the code. All authors contributed to the development of the method, discussion of the results and writing of the manuscript.

DATA AVAILABILITY

KiK-net data are available from the NIED website (https://www.kyoshin.bosai.go.jp; KiK-net data set DOI: https://doi.org/10.17598/nied.0004). The codes used in this study are available from the corresponding author upon reasonable request. All median resonance curves, interferograms and correlograms generated in this study are accessible on Zenodo at the following link: https://doi.org/10.5281/zenodo.17085404. Data processing and visualization were carried out using Python.

REFERENCES

Aguirre, J. & Irikura, K., 1997. Nonlinearity, liquefaction, and velocity variation of soft soil layers in Port Island, Kobe, during the Hyogo-ken Nanbu earthquake, *Bull. seism. Soc. Am.,* **87**(5), 1244–1258.

Aki, K., 1993. Local site effects on weak and strong ground motion, *Tectonophysics,* **218**(1–3), 93–111..

Aoi, S. *et al.*, 2020. MOWLAS: NIED observation network for earthquake, tsunami and volcano, *Earth Planets Space,* **72**(1), 1–31.

Beresnev, I.A. & Wen, K.L., 1996. Nonlinear soil response—A reality?, *Bull. seism. Soc. Am.,* **86**(6), 1964–1978..

Bonilla, L.F. & Ben-Zion, Y., 2020. Detailed space–time variations of the seismic response of the shallow crust to small earthquakes from analysis of dense array data, *Geophys. J. Int.,* **225**(1), 298–310..

Bonilla, L.F., Steidl, J.H., Gariel, J.C. & Archuleta, R.J., 2002. Borehole response studies at the Garner Valley downhole array, southern California, *Bull. seism. Soc. Am.,* **92**(8), 3165–3179.

Bonilla, L.F., Guéguen, P. & Ben-Zion, Y., 2019. Monitoring coseismic temporal changes of shallow material during strong ground motion with interferometry and autocorrelation, *Bull. seism. Soc. Am.,* **109**(1), 187–198.

Boore, D.M. & Bommer, J.J., 2005. Processing of strong-motion accelerograms: needs, options and consequences, *Soil Dyn. Earthq. Eng.,* **25**(2), 93–115.

Boroschek, R.L., Contreras, V., Kwak, D.Y. & Stewart, J.P., 2012. Strong ground motion attributes of the 2010 M_w 8.8 Maule, Chile, earthquake, *Earthq. Spectra,* **28**(1S1), 19–38.

Bustos, J., Pastén, C., Pavez, D., Acevedo, M., Ruiz, S. & Astroza, R., 2023. Two-dimensional simulation of the seismic response of the Santiago Basin, Chile, *Soil Dyn. Earthq. Eng.,* **164,** 107569.

Celebi, M., Dietel, C., Prince, J., Onate, M. & Chavez, G., 1987. Site amplification in Mexico City (determined from 19 September 1985 strong-motion records and from recordings of weak motions), in *Developments in Geotechnical Engineering,* vol. **44,** pp. 141–151, Elsevier.

Chandra, J., Guéguen, P. & Bonilla, L.F., 2014. Application of PGV/VS proxy to assess nonlinear soil response–from dynamic centrifuge testing to Japanese K-NET and KiK-net data, in Proceedings of the *Second European Conference on Earthquake Engineering and Seismology,* European Association for Earthquake Engineering, pp. 25–29.

Dhakal, Y.P., Kunugi, T., Kimura, T., Suzuki, W. & Aoi, S., 2019. Peak ground motions and characteristics of nonlinear site response during the 2018 M_w 6.6 Hokkaido eastern Iburi earthquake, *Earth Planets Space,* **71**(1), 56.

Dhakal, Y.P., Kunugi, T., Kubo, H., Suzuki, W., Shohei, N., Senna, S. & Aoi, S., 2025. Characteristics of peak ground motions and nonlinear site response during the 2024 M_w 7.5 Noto Peninsula earthquake, *Earth Planets Space,* **77**(1), 93.

Ermert, L., Cabral-Cano, E., Chaussard, E., Solano-Rojas, D., Quintanar, L., Morales Padilla, D., Fernandez-Torres, E.A. & Denolle, M.A., 2023. Probing environmental and tectonic changes underneath Ciudad de México with the urban seismic field, *EGUsphere,* **2023,** 1–33.

Esfahani, R., Cotton, F. & Bonilla, L.F., 2024. Temporal variations of the "in-situ" nonlinear behaviour of shallow sediments during the 2016 Kumamoto Earthquake sequence, *Geophys. J. Int.,* **238,** 1626–1637. doi:

Gélis, C. & Bonilla, L.F., 2012. 2-dp–sv numerical study of soil–source interaction in a non-linear basin, *Geophys. J. Int.,* **191**(3), 1374–1390.

Hallo, M., Asano, K. & Iwata, T., 2025. Softening and recovery of near-surface layers during the 2024 M7. 6 Noto earthquake, *J. geophys. Res.: Solid Earth,* **130,** e2024JB029961. doi:

Hardin, B.O. & Drnevich, V.P., 1972. Shear modulus and damping in soils: design equations and curves, *J. Soil Mech. Found. Division,* **98,** doi:.

Idriss, I., 2011. Use of Vs30 to represent local site conditions, in *Proceedings of the 4th IASPEI/IAEE international symposium. Effects of source geology on seismic motion,* International Association of Seismology and Physics of the Earth's Interior, pp. 23–26.

Ishihara, K., 1996. *Soil Behaviour in Earthquake Geotechnics,* Oxford Univ. Press.

Ishihara, K., Yoshida, N. & Tsujino, S., 1985. Modelling of stress-strain relations of soils in cyclic loading, in Proc. of *5th International Conference on Numerical Methods in Geomechanics, Nagoya, Japan,* **Vol. 1,** pp. 373–380.

Kawase, H., Nakano, K., Nagashima, F., Ito, E., Sun, J. & Wang, Z., 2023. Unified approach for evaluation of horizontal site amplification factors with special reference to history of studies on the effects of surface geology on seismic motion, *Earth Planets Space,* **75**(1), 95.

Kokusho, T., 2004. Nonlinear site response and strain-dependent soil properties, *Curr. Sci.-Bangalore-,* **87,** 1363–1369.

Konno, K. & Ohmachi, T., 1998. Ground-motion characteristics estimated from spectral ratio between horizontal and vertical components of microtremor, *Bull. seism. Soc. Am.,* **88**(1), 228–241.

Kramer, S.L., 1996. *Geotechnical Earthquake Engineering,* Pearson Education India.

Lai, S.T. *et al.*, 2025a. Capacity building enables unique near-fault observations of the destructive 2025 M_w 7.7 Myanmar Earthquake, *Earth Syst. Sci. Data Discuss.,* **2025,** 1–23.

Lai, S.T., Schibuola, A. & Bonilla, L.F., 2025b. Unveiling nonlinear site response through time-frequency analysis of earthquake records, *Geophys. J. Int.,* **241,** 1601–1632. doi:

Lee, S.J., Chen, H.W. & Ma, K.F., 2007. Strong ground motion simulation of the 1999 Chi-Chi, Taiwan earthquake from a realistic three-dimensional source and crustal structure, *J. geophys. Res.: Solid Earth,* **112**(B6). doi:.

Liu, Z., Qiao, Y., Cheng, X. & El Naggar, M.H., 2022. Nonlinear seismic response and amplification effect of 3D sedimentary basin based on bounding surface constitutive model, *Soil Dyn. Earthq. Eng.,* **158,** 107292.

Lobkis, O.I. & Weaver, R.L., 2003. Coda-wave interferometry in finite solids: Recovery of *P*-to-*S* conversion rates in an elastodynamic billiard, *Phys. Rev. Lett.,* **90**(25), 254302.

Lu, Y. & Ben-Zion, Y., 2022. Regional seismic velocity changes following the 2019 M_w 7.1 Ridgecrest, California earthquake from autocorrelations and P/S converted waves, *Geophys. J. Int.,* **228**(1), 620–630.

Nakata, N. & Snieder, R., 2011. Near-surface weakening in Japan after the 2011 Tohoku-Oki earthquake, *Geophys. Res. Lett.,* **38**(17). doi:

Nakata, N. & Snieder, R., 2012. Estimating near-surface shear wave velocities in Japan by applying seismic interferometry to KiK-net data, *J. geophys. Res.: Solid Earth,* **117**(B1). doi:
Nakata, N., Snieder, R., Kuroda, S., Ito, S., Aizawa, T. & Kunimi, T., 2013. Monitoring a building using deconvolution interferometry. I: Earthquake-data analysis, *Bull. seism. Soc. Am.,* **103**(3), 1662–1678.
National Research Institute For Earth Science And Disaster Resilience, 2019. NIED K-NET, KiK-net, *Rep. Natl. Res. Inst. Earth Sci. Disaster Resilience*.
Ortiz, F., Pastén, C., Bustos, J., Ruiz, S., Astroza, R. & Easton, G., 2024. Soil amplification in the Santiago city, Chile, due to shallow crustal earthquakes, *Soil Dyn. Earthq. Eng.,* **181,** 108633.
Pasqualini, D., Heitmann, K., TenCate, J.A., Habib, S., Higdon, D. & Johnson, P.A., 2007. Nonequilibrium and nonlinear dynamics in Berea and Fontainebleau sandstones: Low-strain regime, *J. geophys. Res.: Solid Earth,* **112**(B1), e2006JB004264.
Prieto, G.A., Parker, R.L. & Vernon Iii, F., 2009. A Fortran 90 library for multitaper spectrum analysis, *Comput. Geosci.,* **35**(8), 1701–1710.
Qin, L., Ben-Zion, Y., Bonilla, L.F. & Steidl, J.H., 2020. Imaging and monitoring temporal changes of shallow seismic velocities at the Garner Valley near Anza, California, following the M7. 2 2010 El Mayor-Cucapah earthquake, *J. geophys. Res.: Solid Earth,* **125**(1), e2019JB018070.
Régnier, J., Cadet, H., Bonilla, L.F., Bertrand, E. & Semblat, J.F., 2013. Assessing Nonlinear Behavior of Soils in Seismic Site Response: Statistical Analysis on KiK-net Strong-Motion Data, *Bull. seism. Soc. Am.,* **103**(3), 1750–1770..
Régnier, J., Cadet, H. & Bard, P.Y., 2016. Empirical quantification of the impact of nonlinear soil behavior on site response, *Bull. seism. Soc. Am.,* **106**(4), 1710–1719.
Rubinstein, J.L. & Beroza, G.C., 2004. Evidence for widespread nonlinear strong ground motion in the M_w 6.9 Loma Prieta earthquake, *Bull. seism. Soc. Am.,* **94**(5), 1595–1608.
Rubinstein, J.L. & Beroza, G.C., 2005. Depth constraints on nonlinear strong ground motion from the 2004 Parkfield earthquake, *Geophys. Res. Lett.,* **32**(14), e2005GL023189.
Sato, M., Ishikawa, T., Ujihara, N., Yoshida, S., Fujita, M., Mochizuki, M. & Asada, A., 2011. Displacement above the hypocenter of the 2011 Tohoku-Oki earthquake, *Science,* **332**(6036), 1395–1395.
Satoh, T., Horike, M., Takeuchi, Y., Uetake, T. & Suzuki, H., 1997. Nonlinear behaviour of scoria soil sediments evaluated from borehole records in eastern Shizuoka prefecture, Japan, *Earthq. Eng. Struct. Dyn.,* **26**(8), 781–795.
Sawazaki, K. & Snieder, R., 2013. Time-lapse changes of P-and S-wave velocities and shear wave splitting in the first year after the 2011 Tohoku earthquake, Japan: shallow subsurface, *Geophys. J. Int.,* **193**(1), 238–251.
Sawazaki, K., Sato, H., Nakahara, H. & Nishimura, T., 2009. Time-lapse changes of seismic velocity in the shallow ground caused by strong ground motion shock of the 2000 Western-Tottori earthquake, Japan, as revealed from coda deconvolution analysis, *Bull. seism. Soc. Am.,* **99**(1), 352–366.
Schaff, D.P. & Beroza, G.C., 2004. Coseismic and postseismic velocity changes measured by repeating earthquakes, *J. geophys. Res.: Solid Earth,* **109**(B10). doi:
Schimmel, M., 1999. Phase cross-correlations: Design, comparisons, and applications, *Bull. seism. Soc. Am.,* **89**(5), 1366–1378.
Seed, H.B., 1970. *Soil Moduli and Damping Factors for Dynamic Response Analyses,* National Technical Reports Library, Technical Report, EERC–70.
Simons, M. *et al.*, 2011. The 2011 magnitude 9.0 Tohoku-Oki earthquake: mosaicking the megathrust from seconds to centuries, *Science,* **332**(6036), 1421–1425.
Steidl, J.H., Tumarkin, A.G. & Archuleta, R.J., 1996. What is a reference site?, *Bull. seism. Soc. Am.,* **86**(6), 1733–1748.
Stockwell, R., Mansinha, L. & Lowe, R., 1996. Localisation of the complex spectrum: the S transform, *J. Associ. Explor. Geophys.,* **17**(3), 99–114.
Tajima, F., Mori, J. & Kennett, B.L., 2013. A review of the 2011 Tohoku-Oki earthquake (M_w 9.0): Large-scale rupture across heterogeneous plate coupling, *Tectonophysics,* **586,** 15–34.
Takagi, R. & Okada, T., 2012. Temporal change in shear velocity and polarization anisotropy related to the 2011 M9. 0 Tohoku-Oki earthquake examined using KiK-net vertical array data, *Geophys. Res. Lett.,* **39**(9), doi:
TenCate, J.A., Pasqualini, D., Habib, S., Heitmann, K., Higdon, D. & Johnson, P.A., 2004. Nonlinear and nonequilibrium dynamics in geomaterials, *Phys. Rev. Lett.,* **93,** 065501, doi:
Thomson, D.J., 1982. Spectrum estimation and harmonic analysis, *Proc. IEEE,* **70**(9), 1055–1096.
Tong, M., Wang, G.Q. & Lee, G.C., 2005. Time derivative of earthquake acceleration, *Earthq. Eng. Eng. Vibr.,* **4**(1), 1–16.
Ventosa, S., Schimmel, M. & Stutzmann, E., 2017. Extracting surface waves, hum and normal modes: time-scale phase-weighted stack and beyond, *Geophys. J. Int.,* **211**(1), 30–44.
Ventosa, S., Schimmel, M. & Stutzmann, E., 2019. Towards the processing of large data volumes with phase cross-correlation, *Seismol. Res. Lett.,* **90**(4), 1663–1669.
Viens, L., Denolle, M.A., Hirata, N. & Nakagawa, S., 2018. Complex near-surface rheology inferred from the response of greater Tokyo to strong ground motions, *J. geophys. Res.: Solid Earth,* **123**(7), 5710–5729.
Viens, L., Bonilla, L.F., Spica, Z.J., Nishida, K., Yamada, T. & Shinohara, M., 2022. Nonlinear earthquake response of marine sediments with distributed acoustic sensing, *Geophys. Res. Lett.,* **49**(21), e2022GL100122.
Wapenaar, K., Draganov, D., Snieder, R., Campman, X. & Verdel, A., 2010a. Tutorial on seismic interferometry: Part 1—Basic principles and applications, *Geophysics,* **75**(5), 75A195–75A209.
Wapenaar, K., Slob, E., Snieder, R. & Curtis, A., 2010b. Tutorial on seismic interferometry: Part 2—Underlying theory and new advances, *Geophysics,* **75**(5), 75A211–75A227.
Wu, C., Peng, Z. & Ben-Zion, Y., 2009. Non-linearity and temporal changes of fault zone site response associated with strong ground motion, *Geophys. J. Int.,* **176**(1), 265–278.
Wu, C., Peng, Z. & Ben-Zion, Y., 2010. Refined thresholds for non-linear ground motion and temporal changes of site response associated with medium-size earthquakes, *Geophys. J. Int.,* **182**(3), 1567–1576.
Zhang, H., Shi, Y., He, H., Ji, H. & Miao, Y., 2023. Estimating frequency-dependent shear wave velocity in near-surface sediment based on seismic interferometry, *Earth Planets Space,* **75**(1), 167.

APPENDIX A:

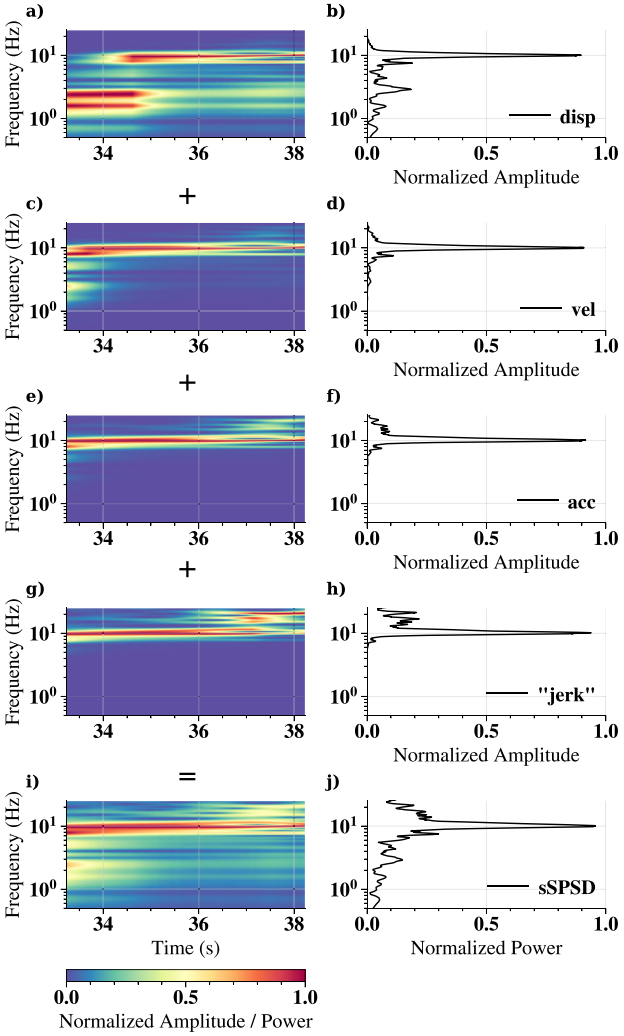

Figure A1. On the left are shown the normalized spectrograms, on the right the respective resonance curves, computed as median of the spectrogram, for a 20.48-s window (transverse component of an event occurred on 2009 November 30 (M_{JMA} 3.5) and recorded by station IWTH14). (a) and (b) show the displacement; (c) and (d), the velocity; (e) and (f), the acceleration; (g) and (h), the jerk; (i) shows the sSPSD, obtained by stacking the individual amplitude spectra, squaring the result, and then renormalizing; and (j) displays corresponding median power spectrum.

A1. Stacked Stockwell power spectral density (sSPSD)

To illustrate the details of the stacked Stockwell power spectral density (sSPSD), we present in Fig. A1 the results for each motion quantity—displacement, velocity, acceleration and jerk—for the same event shown in Fig. 4 (2009 November 30). Each row displays the normalized Stockwell Transform (ST) on the left, and its corresponding amplitude on the right, for one of the quantities (Fig. A1a–h). The results highlight how each derivative emphasizes different parts of the frequency spectrum: displacement focuses on low frequencies, while higher order derivatives (jerk) emphasize high frequencies. Panel (i) shows the spectrogram obtained by stacking the individual amplitude spectra, squaring the result and then renormalizing. Panel (j) presents the corresponding median power spectrum. Notably, the sSPSD spectrum reveals a continuous broad-band distribution, effectively capturing the contributions from all individual representations.

A2. Normalization tests in MDEC and PCC methods

To ensure the recovery of the impulse response function, different normalization strategies were tested during the computation of MDEC and PCC on the inverted signals from the CWT. The three alternative normalization approaches are presented in eqs (1), (A1) and (A2).

The normalization weights are designed to maximize the similarity between the PCC impulse response function and that retrieved from MDEC, without introducing distortions. In addition, the frequency response should remain as consistent as possible not only between MDEC and PCC, but also with the resonance curve obtained from sSPSD.

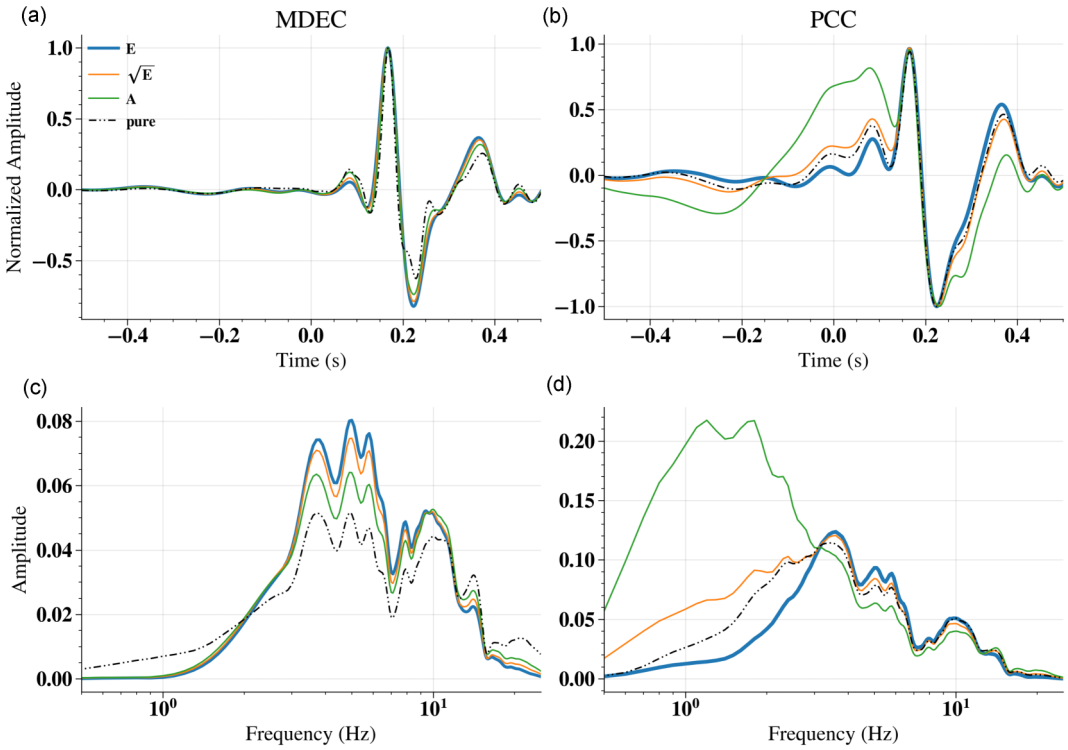

Figure A2. (a) and (b) show the stacked interferograms/correlograms for station IWTH12, transverse component, PGA bin 1–5 cm s^{-2}, (c) and (d) show their spectra. The different colours indicate the type of normalization applied on the interferograms/correlograms: blue for the energy, orange for the square root of the energy, green for the amplitude and in dash-dotted black the case without CWT.

The corresponding results for station IWTH12, transverse component, are shown in Fig. A2, which also includes a comparison case where the CWT is not applied. In the case of MDEC, the different CWT normalizations yield overall comparable results. However, compared to the case without CWT, these normalizations tend to enhance the high-frequency content while reducing the low-frequency content. In contrast, for PCC, using milder normalizations—such as amplitude or the square root of energy—tends to enhance the signal amplitude at negative times and before the tt_{BH} (0.18 s) in the time domain. Simultaneously, in the frequency domain, it results in a stronger concentration of energy at low frequencies. Both effects are more pronounced than in the case without CWT. By applying an energy-based normalization, however, the signal amplitude is reduced in the time domain—particularly before the tt_{BH}—and the low-frequency content is attenuated in the frequency domain. This leads to a better alignment of the PCC spectral peaks with those observed in the MDEC. All results shown in the study adopt the energy-based normalization, as discussed in the main text.

$$\sqrt{E_i} = \sqrt{\sum_t \mathrm{ICWT}_i(t)^2} \tag{A1}$$

$$A_i = \sum_t |\mathrm{ICWT}_i(t)| \tag{A2}$$

A3. Consistency between the frequency content of MDEC, PCC and sSPSD

To assess the consistency among the three independent methods, MDEC, PCC and sSPSD, we compare the frequency content of the estimated impulse response functions obtained from MDEC and PCC with that derived from the sSPSD for two stations, both radial and transverse components. The methods yield coherent results across the frequency domain. The results of this analysis are presented in Fig. A3.

A4. Consistency between MDEC and PCC methods, radial component

To further assess the consistency between the MDEC and PCC methods, we extend the analysis to the radial component (Fig. A4), complementing the transverse component results shown in Fig. 9. Both components show strong agreement between the results obtained from MDEC and PCC.

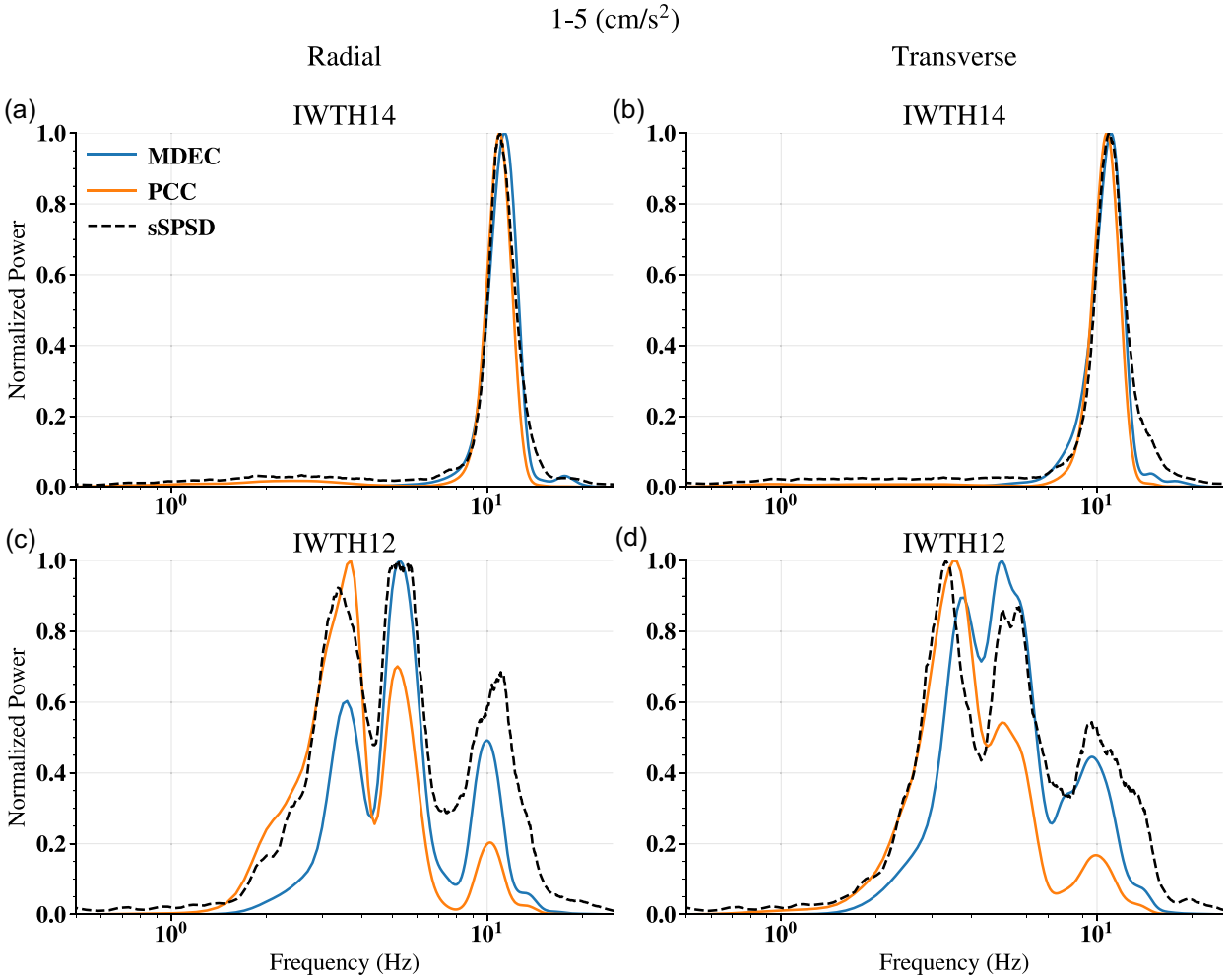

Figure A3. Station IWTH14 (upper panels) and station IWTH12 (lower panels), radial (left) and transverse (right) components. In each panel, the power spectrum resulting from MDEC, PCC and sSPSD methods are shown in blue, orange, dashed black, respectively.

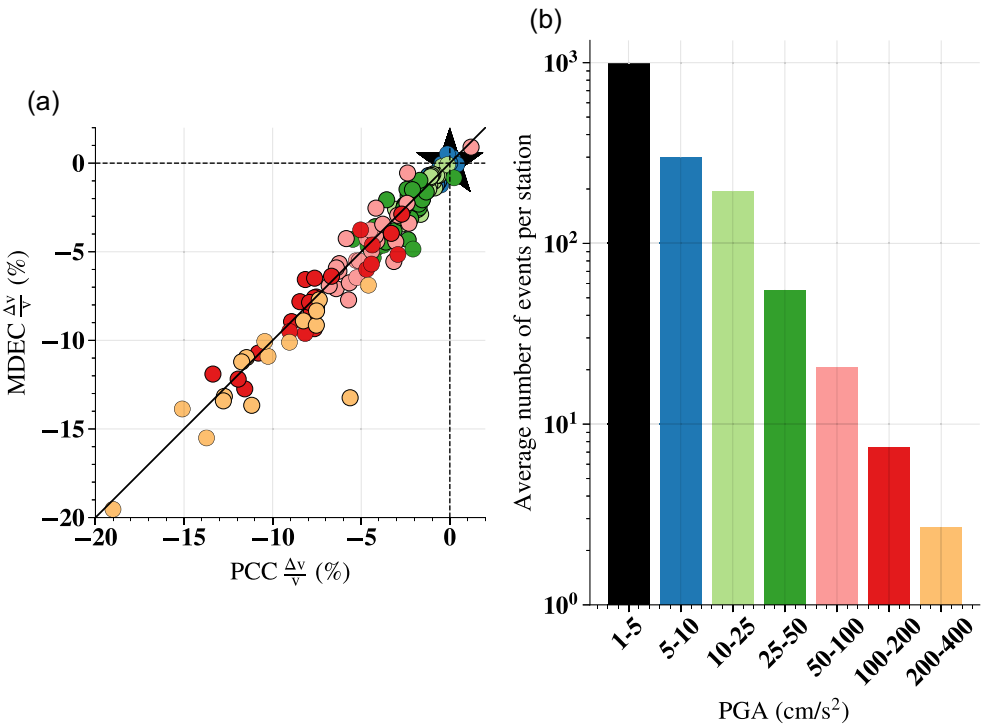

Figure A4. (a) Velocity changes computed with MDEC versus PCC methods using the radial component for all stations in Iwate Prefecture. For each station and each PGA bin larger than 5 cm s^{-2}, velocity change is represented by a dot. The big black star represents the reference PGA bin (1–5 cm s^{-2}). The 1:1 line is represented in black. (b) Average number of events per station for each bin of PGA. For (a) and (b) colours correspond to the PGA bin.

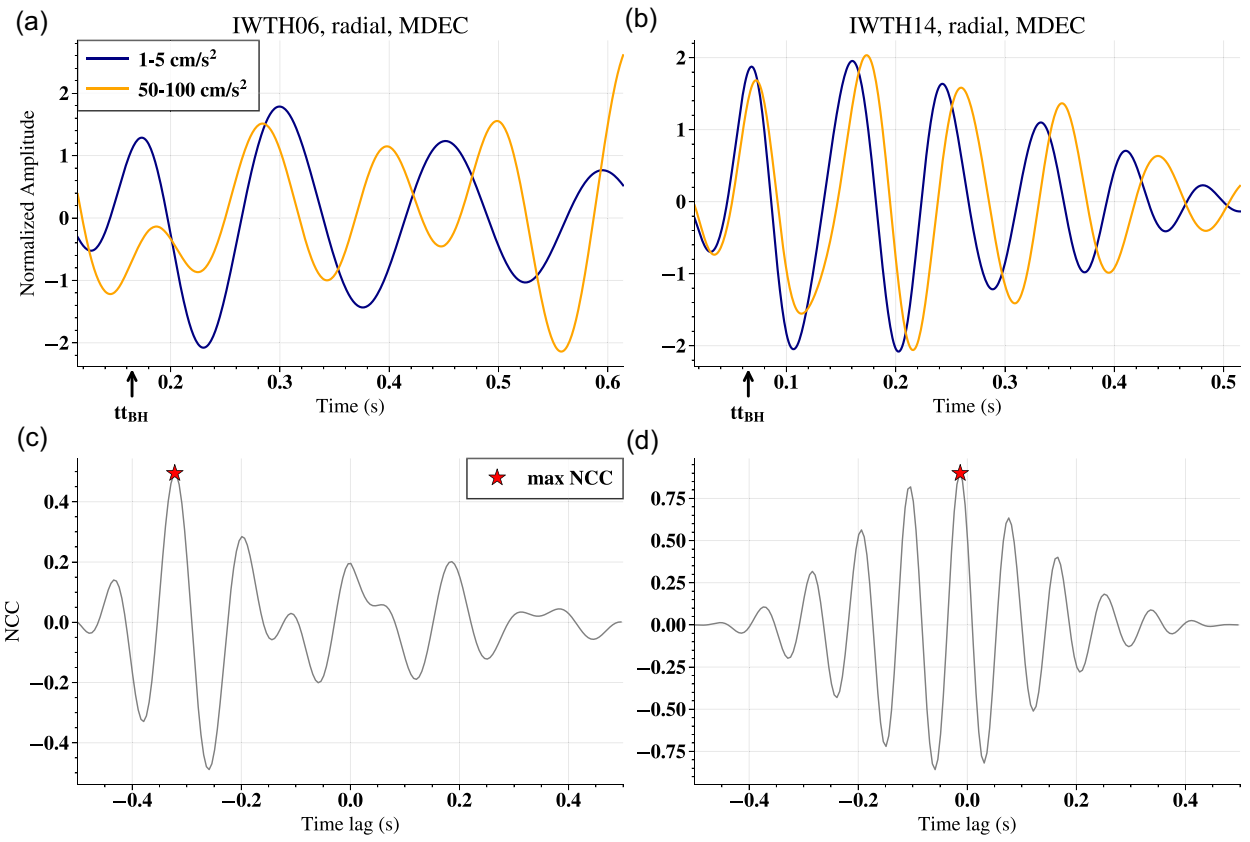

Figure A5. Interferograms 1–5 and 50–100 cm s^{-2} from MDEC method, radial component for station IWTH06 (a), and IWTH14 (b). (a) and (b) Only the time window around tt_{BH} is shown. (c) and (d) resulted normalized cross-correlation (NCC) between the two windowed interferograms in (a), and in (b), respectively. The maximum value of NCC is indicated with a star.

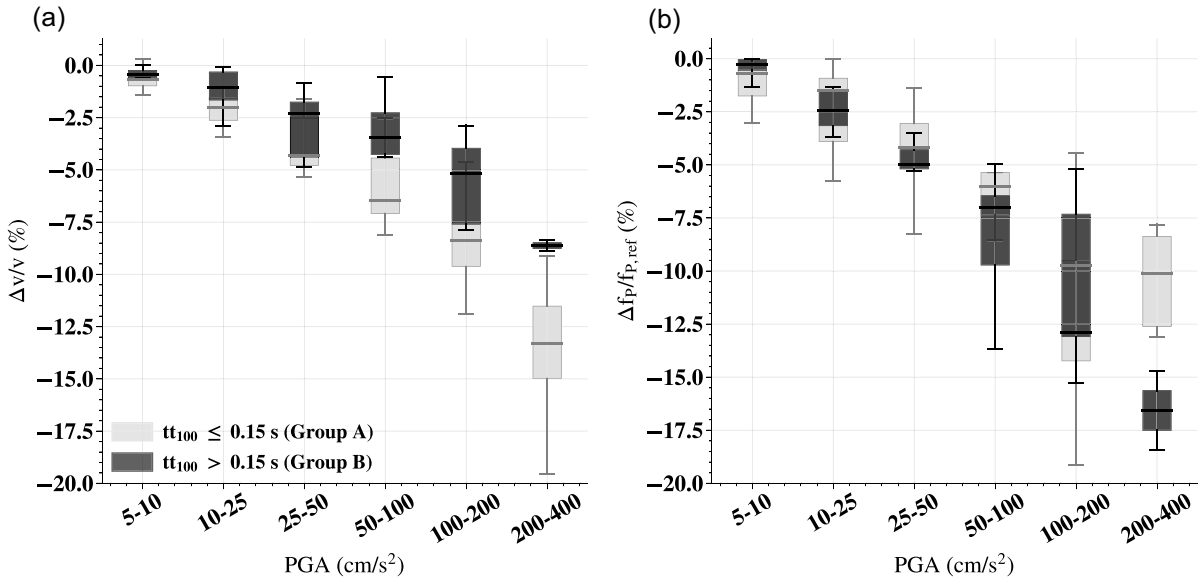

Figure A6. For each PGA bin, (a) shows velocity changes obtained using the stretching method on the radial component of stacked interferograms, and (b) shows frequency changes obtained from the f_P shift between the median resonance curves. Both (a) and (b) measure the velocity/frequency changes with respect to the reference 1–5 cm s^{-2} PGA bin (not shown in the plots). The grey and black boxes indicate the interquartile ranges, with the lines inside representing the medians: grey for group A ($tt_{100} \leq 0.15$ s) and black for group B ($tt_{100} > 0.15$ s). The whiskers extend to the most extreme data points within 1.5 times the interquartile range.

A5. Selection criteria of interferograms/correlograms before stretching

In Figs A5(c) and A5(d), we compute the normalized cross-correlation (NCC) between the reference interferogram/correlogram (1–5 cm s^{-2}) and a current one (50–100 cm s^{-2}) within the selected time window. The NCC is evaluated for time-shifts of 0.01 s on both sides of the reference trace, and the time lag is taken from the shift corresponding to the maximum NCC. An interferogram/correlogram is retained only if the maximum NCC is ≥ 0.85 and the associated time lag is ≤ 0.05 s (10 per cent of the window length). Based on these criteria, the 50–100 cm s^{-2} interferogram for the radial component at station IWTH06 is rejected. In Fig. A5, the left panels illustrate this rejected case, while the right panels show a retained example from station IWTH14. For IWTH06, the lag time associated with the maximum NCC is approximately –0.32 s. However, inspection of the reference and current interferograms (Figs A5a and c) reveals no consistent delay of the current trace relative to the reference. Instead, the maximum NCC corresponds to two peaks that are not temporally aligned. The peak in the current interferogram matches an earlier, unrelated peak in the reference rather than its true counterpart. In contrast, the current interferogram of IWTH14 (Fig. A5b) exhibits a delay that progressively increases over time, with the five visible peaks within the selected window closely aligned between the reference and current traces. The lag time corresponding to the maximum NCC is approximately –0.013 s (Fig. A5d), in good agreement with the median delay observed in Fig. A5(b).

A6. Velocity and frequency changes versus PGA bin for the radial component

Resulting $\Delta v/v$ and $\Delta f_P/f_{P,\mathrm{ref}}$ values across PGA bins for the radial component are shown in Fig. A6. As in the complementary Fig. 10 in the main text, grey boxes represent stations of group A ($tt_{100} \leq 0.15$ s), while black boxes correspond to stations of group B ($tt_{100} > 0.15$ s). Velocity changes are greater for group A—similar to the transverse component, but with a more pronounced gap between the two station families—whereas frequency changes show no consistent separation (Fig. A6).